JETP Letters, Vol. 71, No. 11, 2000, pp. 447–450. Translated from Pis'ma v Zhurnal Éksperimental'noĭ i Teoreticheskoĭ Fiziki, Vol. 71, No. 11, 2000, pp. 657–662.


# Experimental Estimation of the Possible Subbarrier Penetration of Ultracold Neutrons through Vacuum-Tight Foils

**E. V. Lychagin*, A. Yu. Muzychka*, V. V. Nesvizhevsky**, G. V. Nekhaev*, and A. V. Strelkov***

** Joint Institute for Nuclear Research, Dubna, Moscow region, 141980 Russia*

*e-mail: lychag@nf.jinr.ru*

*** Institute Laue–Langevin, Grenoble, 38042 France*

Received April 21, 2000

The probability of subbarrier penetration of ultracold neutrons through 15 μm-thick vacuum-tight beryllium foil (boundary energy for beryllium is $E_{\text{lim Be}} = 249$ eV) was measured. It is equal to $(-1.2 \pm 1.0) \times 10^{-8}$ per collision of neutrons with energy lower than ~160 neV. © *2000 MAIK "Nauka/Interperiodica".*

PACS numbers: 28.20.-v

At present, the investigation of an anomaly (large discrepancy between the calculated and experimental storage times [1]) in ultracold neutron (UCN) storage in isolated vessels has become a problem of no less interest than even the supposed use of prolonged UCN storage for some fundamental experiments. The anomaly in UCN storage was examined in a series of experiments carried out to reveal the ways of UCN leakage from vessels. In principle, one of the supposed channels of UCN leakage could be subbarrier UCN penetration through, or into, the vessel walls. The UCN penetration through beryllium foil observed in experiment [2] was caused by a partial heating of stored UCN [3, 4] and, hence, by the ordinary above-barrier UCN passage through the foil.

A more recent experiment [5] revealed the UCN leakage through deposited 0.2- to 3-μm layers of beryllium, zirconium, and nickel–molybdenum alloy, which could be explained by the presence of micropores in the deposited layers. The presence of such technologic imperfections could not be established by a mere check for the vacuum tightness of layers, because the layers were deposited on an aluminum base. Moreover, this experiment was characterized by the presence of a basically unremovable background of the UCNs, whose energies slightly increased during the storage [3, 4]. This background restricted, to a level of $\sim 10^{-6}$, the sensitivity of the method to the probability of penetration per collision with the layer surface.

Recent theoretical studies [6–9] predicted that UCN penetration through the potential barrier can be much more efficient than the quantum-mechanical tunneling effect.

To clarify the problem of UCN penetration through the walls (at least, to determine the role of this process in the UCN storage anomaly), we performed an experiment in which the accuracy of determining the upper limit of the probability of subbarrier penetration through a thin foil was improved by two orders of magnitude.

**1.** Figure 1 shows the scheme of the experimental apparatus. Ultracold neutrons are delivered from the source to the apparatus through the stainless-steel neutron guide *1*. Neutrons irradiate vacuum-tight 15-μm beryllium foil *2* covering an area of 63 $\text{cm}^2$ and separating the inlet neutron guide from the storage vessel *3*. The inlet neutron guide may be closed by gate *4*, which excludes the fall of slow neutrons with any energies from the neutron guide into the apparatus.

The storage vessel was a copper sphere 39 cm in diameter, with the copper rotating shutter *5* at the outlet for keeping UCN within the vessel. The spherical storage vessel was evacuated to a residual gas pressure of $\sim 10^{-3}$ mbar for six hours at temperature 110–150°C.

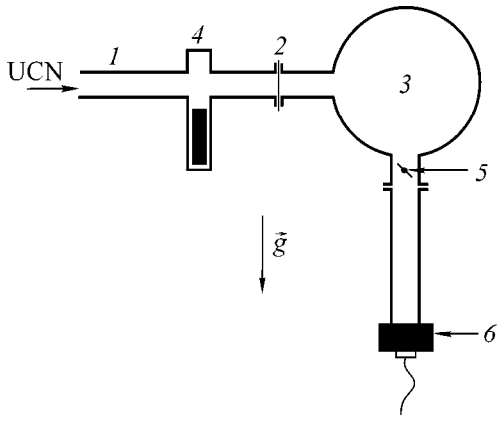


**Fig. 1.** Scheme of the apparatus: (*1*) inlet neutron guide, (*2*) beryllium foil, (*3*) storage vessel, (*4*) gate, (*5*) rotating shutter, (*6*) UCN detector.

0021-3640/00/7111-0447$20.00 © 2000 MAIK "Nauka/Interperiodica"

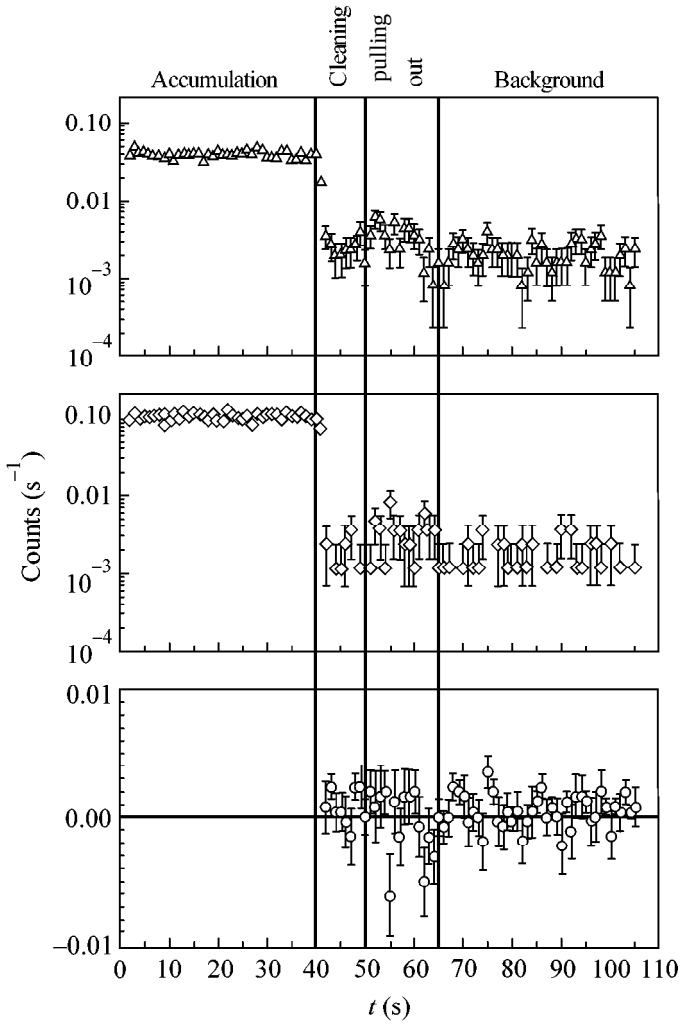


**Fig. 2.** Time dependence of the detector counting rate: (triangles) in measurements with 15-μm beryllium foil at the inlet; (rhombi) in measurements with 15-μm beryllium and 14-μm copper foils at the inlet; and (circles) the difference between the two measurements from which the respective backgrounds were subtracted.

The ultracold-neutron detector *6*—a gas-discharge counter with $^3$He (pressure ~10 torr) and a thin (100 μm) aluminum window—was connected through a neutron guide, similar to the inlet guide, with the storage vessel outlet in the lower part of the sphere. The detector was situated ~60 cm lower than the bottom of the storage vessel and surrounded by neutron shielding made from cadmium and boron-containing rubber. The electronic efficiency of neutron detection was ~80%, and the background at the closed gate was equal to $(8.8 \pm 0.6) \times 10^{-4}$ s$^{-1}$. The detector operation during the measurements was controlled by the amplitude analyzer.

**2.** The idea of the experiment was that the neutrons penetrating through the potential barrier of the foil could be accumulated in the storage vessel. The above-barrier (for the beryllium foil) neutrons easily penetrating through the foil could not be accumulated, because the boundary energy of the foil far exceeded the boundary energy of the storage vessel walls ($E_{\text{lim Be}}$ = 249 neV, $E_{\text{lim Cu}}$ = 168 neV). Knowing the number of neutrons accumulated in the storage vessel during the time $\Delta t$, the neutron flux with energy below $E_{\text{lim Cu}}$ on the surface of the inlet foil for the same time $\Delta t$, the time of neutron storage in the vessel, and the time of filling and pulling out, one can determine the probability of subbarrier UCN penetration through the foil per single collision.

The measurement procedure consisted of the following cyclically repeated sequence:

(i) The gate is opened (the outlet shutter is closed) and the UCN flux irradiates the beryllium foil for $\Delta t_{\text{fill}}$ = 40 s. Neutrons, including those penetrating through the potential barrier of the foil, are accumulated.

(ii) The gate is closed and, during the time interval of $\Delta t_{clear} = 10$ s, the storage vessel is cleared of neutrons with energies exceeding the boundary energy of the vessel walls (neutrons having energies higher than $E_{lim\ Cu}$ and penetrating into the vessel can undergo several collisions with the walls before leaving the storage vessel).

(iii) The outlet shutter is opened, and the accumulated neutrons, if present, are pulled out from the storage vessel to the detector during the time $\Delta t_{empty} = 15$ s.

(iv) Shutter is closed, and the detector background is counted for the next 40 s.

For control, a similar measurement was carried out with a 14-μm copper foil mounted behind the beryllium foil. This foil reduced by many orders the probability of the subbarrier (for copper) neutrons penetrating into the storage vessel but virtually did not affect the high-energy neutrons and, therefore, any processes associated with these neutrons and leading to the systematic error. The differential measurement allowed these errors to be obviated.

To determine the UCN flux with energy below $E_{lim\ Cu}$ incident on the beryllium foil, the inlet and outlet of the storage vessel were interchanged and the foil at the new outlet was replaced by a thick copper membrane with a small (0.21 $cm^2$) aperture, through which the UCN density in the storage vessel was monitored. From a change in the detector counting rate in the course of filling, one could derive the filling constant $\tau_{fill}$ for the storage vessel, while, after the gate and the shutter were closed, the storage time constant $\tau_{stor}$ could be determined. After determining the neutron density (5 UCN/$cm^2$) in the storage vessel at the instant the inlet gate was closed, the flux of neutrons with energies below $E_{lim\ Cu}$ at the apparatus inlet was obtained by extrapolating the storage curve to the corresponding time $t$ with known $\tau_{fill}$ and $\tau_{stor}$. The time of pulling out the stored neutrons was determined in a separate measurement (without a membrane at the outlet).

**3.** The top and middle panels in Fig. 2 show the detector counting rates obtained during the cycle in the measurements with beryllium foil and with jointly mounted beryllium and copper foils, respectively. The difference in the fluxes of "above-beryllium" neutrons penetrating into the detector in the course of filling (first 40 s) is due to the fact that the aperture in the outlet shutter was increased in the second measurement. This increase was of an engineering character and did not affect the results. The bottom panel in Fig. 2 shows the difference between these two measurements, from which the respective backgrounds were preliminarily subtracted.

The measurements with only the beryllium foil and with two (beryllium and copper) foils at the inlet gave, respectively, the values of $(1.0 \pm 0.2) \times 10^{-2}$ and $(1.6 \pm 0.4) \times 10^{-2}$ neutron/cycle for the number of neutrons accumulated per cycle. From the difference between these measurements and with allowance made for the loss of accumulated neutrons during the time intervals $\Delta t_{clear}$ and $\Delta t_{empty}$, the value of $(-1.2 \pm 1.0) \times 10^{-8}$ per collision with the surface of the beryllium foil was obtained for the probability of subbarrier penetration for neutrons with energies in the range ~(40–160) neV (the lower limit was caused by the properties of the UCN source).

**4.** A number of processes introduced systematic error into this experiment.

First, some of the neutrons with energies below $E_{lim\ Cu}$ avoided the foil potential barrier and penetrated into the storage vessel either through microholes in the foil or by bypassing the foil. In the experiment, the foil vacuum tightness was checked with a helium leak detector. The value of $\sim 1.5 \times 10^{-14}$ $cm^{-2}$ obtained for the possible hole area entirely excludes the direct passage through microholes. Neutron penetration through the teflon seal and air gap around the foil was not excluded, in principle.

Second, the UCN cooling process recently discovered in [10, 11] should lead to a systematic increase in the rate of counting accumulated neutrons. The above-beryllium neutrons easily penetrating through the foil can reduce their energy to energies lower than $E_{lim\ Cu}$ when they leave the foil or collide with the opposite wall of the storage vessel.

The gate is opened and closed with a marked impact effect on the apparatus. Moreover, in practical measurements, a rotating shutter, similar to the outlet shutter, was situated after the foil at the inlet to the storage vessel and was opened only for the filling time. The cooling of the above-barrier neutrons upon their interaction with the storage vessel walls at the time of gate impact or upon the interaction with the rapidly moving shutter can also introduce systematic error.

The above-listed systematic effects (except those related to the foil microholes, whose area was experimentally estimated) were all compensated in our experiment, because the penetration probability was determined from the difference between two measurements: with one beryllium foil and with two (beryllium and copper) foils at the inlet. In addition, special measurements with a slowly rotated shutter yielded a value of $(1.5 \pm 0.5) \times 10^{-2}$ neutron/cycle, which coincided, within the statistical errors, with the results obtained with a rapidly moving shutter.

**5.** The method used in this work is likely the most sensitive to the subbarrier UCN penetration through thin films. After removing the above-mentioned systematic errors, the direct, instead of difference, measurement will allow the accuracy to be increased by more than an order of magnitude, all other factors being the same. Further increase in accuracy of such a measurement is possible with the use of a larger foil surface irradiated by neutrons, an increase in the neutron storage time, a decrease in the detector background, and

with the use of a higher UCN flux. To analyze the penetration of neutrons with energies close to the potential barrier boundary, the method described in this work can be employed on an apparatus of the gravitational spectrometer type described in [10].

The upper limit $(-1.2 \pm 1.0) \times 10^{-8}$ obtained in this work for the probability of direct penetration through the barrier is well below the probability ($\sim 10^{-5}$ per impact) of anomalous losses in beryllium.

As a rule, the hypotheses explaining the anomalously large on-beryllium losses in UCN storage by subbarrier penetration say nothing about the behavior of a neutron whose kinetic energy is less than the potential barrier height but which, nevertheless, falls into the subbarrier region. Since the neutron lifetime under the barrier may be considerably shorter than the penetration time, the absence of penetration through foils can be explained by different theoretical hypotheses. At present, attempts at measuring the probability of anomalous subbarrier penetration of cold neutrons into (and not through) the barrier are underway [12]. However, the present experimental accuracy is at the level of $10^{-4}$.

The experiment was carried out on the ILL reactor (Grenoble, France), PF2 instrument. We are grateful to P. Geltenbort, Th. Brenner, and the operating staff for assistance.

## REFERENCES

1. V. P. Alfimenkov, V. V. Nesvizhevskiĭ, A. P. Serebrov, *et al.*, Pis'ma Zh. Éksp. Teor. Fiz. **55**, 92 (1992) [JETP Lett. **55**, 84 (1992)].
2. V. E. Varlamov, P. Gel'tenbort, V. V. Nesvizhevskiĭ, *et al.*, Pis'ma Zh. Éksp. Teor. Fiz. **66**, 317 (1997) [JETP Lett. **66**, 336 (1997)].
3. V. V. Nesvizhevsky, P. Geltenbort, A. V. Strelkov, *et al.*, ILL Annual Report 97.
4. V. V. Nesvizhevskiĭ, A. V. Strelkov, P. Gel'tenbort, *et al.*, Yad. Fiz. **62**, 832 (1999) [Phys. At. Nucl. **62**, 776 (1999)]; Preprint No. R-98-79, OIYaI (JINR, Dubna, 1998).
5. P. Geltenbort, D. G. Kartashov, A. G. Kharitonov, *et al.*, ILL Experimental Report, No. 3, 146, 1998.
6. A. P. Serebrov, in *Proceedings of the 5th International Seminar on Interactions of Neutrons with Nuclei, Dubna, 1997* (JINR), p. 67.
7. V. K. Ignatovich and M. Utsuro, Phys. Lett. A **225**, 195 (1997).
8. V. G. Nosov and A. Frank, Phys. Rev. A **55**, 1129 (1997).
9. Yu. A. Alexandrov, in *Proceedings of the 7th International Seminar on Interactions of Neutrons with Nuclei, ISIN-7, Dubna, 1999* (JINR), p. 282; Hadronic J. **23** (2000) (in press).
10. A. V. Strelkov, V. V. Nesvizhevsky, P. Geltenbort, *et al.*, Nucl. Instrum. Methods Phys. Res. A **440**, 695 (2000); Pis'ma Zh. Éksp. Teor. Fiz. **70**, 175 (1999) [JETP Lett. **70**, 170 (1999)]; Preprint No. R-3-99-71, OIYaI (JINR, Dubna, 1999).
11. S. Arzumanov, L. Bondarenko, S. Chernyavsky, *et al.*, in *Proceedings of the 6th International Seminar on Interactions of Neutrons with Nuclei, ISIN-6, Dubna, 1998*, p. 108.
12. M. Utsuro and V. K. Ignatovich, Phys. Lett. A **246**, 7 (1998).

*Translated by R. Tyapaev*

JETP Letters, Vol. 71, No. 11, 2000, pp. 451–452. Translated from Pis'ma v Zhurnal Éksperimental'noĭ i Teoreticheskoĭ Fiziki, Vol. 71, No. 11, 2000, pp. 663–665.


# Isotope Effect in Nuclear Capture of Negative Muons in Xenon

**T. N. Mamedov, V. G. Grebinnik, K. I. Gritsaĭ, V. N. Duginov, V. A. Zhukov, V. G. Ol'shevskiĭ, and A. V. Stoĭkov**

*Joint Institute for Nuclear Research, Dubna, Moscow region, 141980 Russia*

*e-mail: tmamedov@nu.jinr.ru*

Received May 10, 2000

The lifetime of negative muons in the $^{129}$Xe 1*s* state was measured. The muon capture rate in $^{129}$Xe is compared with that in the $^{132, 136}$Xe isotopes. The capture rate was found to depend on the mass number of the cited isotopes. The experimental results are compared with the results of calculations by the semiempirical Goulard–Primakoff formula. © *2000 MAIK "Nauka/Interperiodica".*

PACS numbers: 23.40.-s; 27.60.+j

It was predicted in early theoretical works [1–3] on nuclear capture of negative muons $\mu^- + (Z, A) \longrightarrow (Z - 1, A)^* + \nu_\mu$ ($Z$ and $A$ are the nuclear charge and mass number, respectively) that the muon capture rates can differ for different isotopes of the same element. In the cited works, the isotope effect was predicted irrespective of the nucleus model used in calculations.

The general behavior of the muon capture rate by nuclei differing in $Z$ and $A$ is described by the semiempirical Goulard–Primakoff formula [4], according to which the capture rate decreases with increasing neutron excess $(A - Z)/2A$ in nuclei with identical $Z$. This effect was experimentally observed for several nuclei [5]. In some works, the data were obtained only for two nuclei differing in $A$ and having the same $Z$, which did not permit the functional form of the capture rate to be determined over a wide range of neutron excess numbers. Samples with an insufficient isotope purity were also used in some works, rendering their results less valuable.

More reliable data for checking the isotope effect were obtained in [6], where four chromium isotopes ($^{50, 52, 53, 54}$Cr) and three nickel isotopes ($^{56, 60, 62}$Ni) were examined. The results of that work did not contradict the Primakoff prediction [3] and agreed well with the results of theoretical studies [7, 8], in which the shell model was used and the residual nucleon interaction in nuclei was taken into account.

This work reports a summary of negative muon capture rates in $^{129, 132, 136}$Xe isotopes. The capture rates in $^{132, 136}$Xe were measured in our previous works [9, 10]. Xe has nine stable isotopes, permitting the isotope effect to be measured over a wide range of mass numbers. In this work, the results are presented for three isotopes having the highest natural abundances.

The experiments were carried out using conventional $\mu SR$ technique and consisted of measuring the total rate of muon disappearance from the 1*s* state by detecting the $\mu^- \longrightarrow e^-$ decay electrons for the isotope of interest. Frozen solid xenon samples were used. The purity of the samples was as follows:

$^{129}$Xe—99.91%, $^{128}$Xe—0.08%;

$^{132}$Xe—95.1%, $^{131}$Xe—4.9%;

$^{136}$Xe—94%, $^{134}$Xe—5.9%.

Least-squares fit to the experimental data was carried out using the formula (the external magnetic field was less than $10^{-2}$ Oe)

$$N(t) = \sum_{i=1}^{3} N_i(0)\exp(t/\tau_i) + Bg, \qquad (1)$$

where $N_i(0)$ are the electron counts at $t = 0$; $\tau_{1, 2, 3}$ are the muon lifetimes in the Xe, Al, and C 1*s* states, respectively (Al and C are present in the walls of the target chamber and in the scintillators); and $Bg$ is the accidental background comprising approximately 0.15% of the total contribution from the $N_i(0)$ components. The muon lifetimes in Al and C were taken from the tabulated data [5]: $\tau(\mathrm{Al}) = 864.0 \pm 2.0$ ns, and $\tau(\mathrm{C}) = 2026.3 \pm 1.5$ ns.

The spins of the $^{132}$Xe and $^{136}$Xe nuclei are zero, and $^{129}$Xe has a spin of $J = 1/2$. In the muonic atom formed by the nucleus with nonzero magnetic moment, the muonic 1*s* level splits into two hyperfine components with total angular momenta $F^+ = J + 1/2$ and $F^- = J - 1/2$. The time distribution of decay electrons for the muons occupying these states is given by the formula [12]

$$N_e(t) \sim (1 - A_e\exp(-Rt))\exp(-\Lambda^- t), \qquad (2)$$

where $A_e = n^+(0)\Delta\Lambda/R$, $n^+(0)$ is the upper state population at $t = 0$, $\Delta\Lambda$ is the difference in the rates of muon disappearance from the two hyperfine states, $R$ is the transition rate between these states, and $\Lambda^-$ is the rate of

**Table**

| Isotope | τ, ns | | $\Lambda_c$, $\mu s^{-1}$ | |
|---|---|---|---|---|
| | experiment | calculated by [4] | experiment | calculated by [4] |
| $^{129}$Xe | 82.7 ± 1.7 | 82.9 | 11.7 ± 0.3 | 11.6 |
| $^{132}$Xe | 101.7 ± 1.7 [10] | 97.8 | 9.4 ± 0.2 [10] | 9.8 |
| $^{136}$Xe | 111.0 ± 4.6 [9] | 125.4 | 8.6 ± 0.4 [9] | 7.5 |

muon disappearance from the lower state. In an analysis of the data on muon capture by the $^{129}$Xe nucleus, the spectra were also processed using Eq. (1), because $A_e < 10^{-4}$ and $R > 10^8$–$10^9$ $s^{-1}$ for heavy nuclei [12].

The rate $\Lambda_c$ of muon capture by the Xe nuclei was calculated using the formula $\tau^{-1} = Q\Lambda_d + \Lambda$, where $\Lambda_d$ is the free muon decay rate (taken equal to the inverse $\mu^+$ lifetime 2197.03 ± 0.04 ns [13]) and $Q = 0.91$ is the decay suppression factor for the bound muon [14].

The experimentally measured lifetimes of negative muons in the $^{129, 132, 136}$Xe isotopes and the rates of muon capture by the nuclei of these isotopes are given in the table. The calculated capture rates, as predicted by the Goulard–Primakoff formula [4], are also given in the table.

A comparison of the experimental and calculated capture rates of negative muons in the $^{129, 132, 136}$Xe isotopes is shown in the figure. An appreciable isotope effect is observed for the capture rate in the xenon isotopes. Its dependence on the isotope mass number is satisfactorily described by the semiempirical Goulard–Primakoff formula [4].

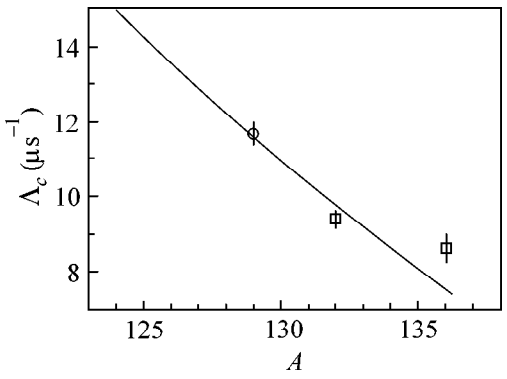


Mass-number dependence of the negative muon nuclear capture rate in the $^{129, 132, 136}$Xe isotopes: (○) this work; (□) data from [9, 10]; the solid line corresponds to the calculation by the Goulard–Primakoff formula [4].

We are grateful to the Directorate of the Laboratory of Nuclear Problems of the Joint Institute for Nuclear Research for attention and assistance. We are also grateful to A.V. Dem'yanov for assistance in measurements. This work was supported by the Russian Foundation for Basic Research, project no. 96-02-17582.

## REFERENCES

1. J. M. Kennedy, Phys. Rev. **87**, 953 (1952).
2. H. A. Tolhoek and J. R. Luyten, Nucl. Phys. **3**, 679 (1957).
3. H. Primakoff, Rev. Mod. Phys. **31**, 802 (1959).
4. B. Goulard and H. Primakoff, Phys. Rev. C **10**, 2034 (1974).
5. T. Suzuki, D. F. Measday, and J. P. Roalsvig, Phys. Rev. C **35**, 2212 (1987).
6. V. Bobrov, V. Varlamov, Yu. Grashin, *et al.*, Yad. Fiz. **4**, 75 (1966) [Sov. J. Nucl. Phys. **4**, 53 (1967)].
7. G. G. Bunatyan, Yad. Fiz. **2**, 868 (1965) [Sov. J. Nucl. Phys. **2**, 619 (1966)].
8. V. M. Novikov and M. G. Urin, Yad. Fiz. **3**, 419 (1966) [Sov. J. Nucl. Phys. **3**, 302 (1966)].
9. T. N. Mamedov, V. G. Grebinnik, V. A. Zhukov, *et al.*, Pis'ma Zh. Éksp. Teor. Fiz. **67**, 302 (1998) [JETP Lett. **67**, 318 (1998)].
10. T. N. Mamedov, V. G. Grebinnik, K. I. Gritsaĭ, *et al.*, Pis'ma Zh. Éksp. Teor. Fiz. **69**, 181 (1999) [JETP Lett. **69**, 192 (1999)].
11. T. N. Mamedov, V. G. Grebinnik, K. I. Gritsaĭ, *et al.*, Preprint No. R15-96-498, OIYaI (JINR, Dubna, 1996).
12. R. Winston, Phys. Rev. **129**, 2766 (1963).
13. Particle Data Group, Review of Particle Physics, Eur. Phys. J. C **3**, 1 (1998).
14. R. W. Huff, Ann. Phys. (Leipzig) **16**, 288 (1961).

*Translated by V. Sakun*

JETP Letters, Vol. 71, No. 11, 2000, pp. 453–456. Translated from Pis'ma v Zhurnal Éksperimental'noĭ i Teoreticheskoĭ Fiziki, Vol. 71, No. 11, 2000, pp. 666–670.


# Dynamics of the Spatial Spectrum of a Self-Focusing Optical Wave in a Nonlinear Medium

**S. A. Iz"yurov and S. A. Kozlov**

*Institute of Fine Mechanics and Optics, ul. Sablinskaya 14, St. Petersburg, 197101 Russia*

*e-mail: izyurov@infopro.spb.su, kozlov@phd.ifmo.ru*

Received April 28, 2000

A new nonlinear equation for the dynamics of the spatial spectrum of a self-focusing monochromatic wave in a medium with cubic nonlinearity is derived in the nonparaxial approximation. The formation of optical beams with cross section on the order of a wavelength is considered. Backward self-reflection is found to be the fundamental cause for the limitation of optical self-focusing. *© 2000 MAIK "Nauka/Interperiodica".*

PACS numbers: 42.65.Jx

Self-focusing in media with positive nonlinearity of the refractive index is a classical phenomenon of nonlinear optics. Since the early 1960s, hundreds of publications have been devoted to this phenomenon. An excellent and detailed review of these works is given, e.g., in monograph [1]. In most of them, the theory of monochromatic radiation self-focusing in isotropic media was based on an analysis of the solutions of the cubic Schrödinger equation, to which the Maxwell equations are reduced in the approximation of paraxial optical beams. However, the theoretical description in this approximation leads to the catastrophic character of self-focusing with field collapse into a point. The behavior of a light field in the vicinity of a singularity, where the paraxial approximation does not apply, was analyzed in many works and also reviewed in [1]. Rigorous solutions of the Maxwell equations for isotropic media with cubic nonlinearities were obtained only for the stationary (i.e., in the terminology of [1], independent of the coordinate along the light propagation axis) nonparaxial optical beams (see also [2] and the review given therein). The nonstationary (in the above-mentioned sense) field evolution in the course of a deep self-focusing was studied on the basis of various modifications of Schrödinger equations. A critical review of the approximations used in these treatments is given, e.g., in [3]. Note, for our part, that, in the majority of works, a rigorous description was not suggested even for the linear diffraction of narrow optical beams. Although linear nonparaxial diffraction was correctly treated in [4] (this is likely the most popular work on nonparaxial self-focusing), the vector character of the three-dimensional nonlinear field evolution was not taken into account in [4], rendering the treatment incorrect on this point [1, 2].

In this work, a new nonlinear equation is derived for the nonparaxial self-focusing of monochromatic radiation in an isotropic medium with cubic nonlinearity. It describes the evolution of the spatial spectrum of an optical beam rather than the evolution of its field. When linearized, this equation exactly describes the diffraction of a unidirectional wave, including the situation where its spatial spectrum involves the components with spatial frequencies greater than the wave number and corresponding to the evanescent waves instead of the traveling waves. The method of deriving the spectral equation is based on the requirement that its solutions of unidirectional wave type be partial solutions of the nonreduced nonlinear wave equation. The reduced wave equation, an analogue of the spectral equation derived in this work, is nontrivial. This is probably the reason why it was not obtained for a rather long time. Numerical analysis of the new solutions is used to discuss the ultrabroadening of the spatial spectrum of radiation and the formation of a self-focusing beam with a cross section on the order of a wavelength. It is shown that the backward self-reflection of radiation may be the natural reason for preventing self-focusing collapse.

In describing the propagation of monochromatic radiation in an isotropic dielectric medium with cubic nonlinearity, the Maxwell equations can be reduced to the form [1]

$$\nabla \times (\nabla \times \mathbf{E}) - k_0^2 \mathbf{D} = 0, \qquad (1)$$

where $\mathbf{E}$ is the complex amplitude of electric field $\mathbf{E}' = \frac{1}{2}\mathbf{E}\exp(-i\omega t)$ + c.c. of the optical wave; $\mathbf{D} = \epsilon\mathbf{E} + 12\pi\chi^{1111}(\mathbf{E}\mathbf{E}^*)\mathbf{E} + 12\pi\chi^{1221}\mathbf{E}\times(\mathbf{E}^*\times\mathbf{E})$ is the complex amplitude of electric induction $\mathbf{D}' = \frac{1}{2}\mathbf{D}e^{-i\omega t}$ + c.c.; $\omega$ is the light frequency; $k_0 = \omega/c$ is the wave number in vacuum; $\epsilon$ is the dielectric constant of the medium; $\chi^{1111}$ and $\chi^{1221}$ are the tensor components of its nonlinear sus-

0021-3640/00/7111-0453$20.00 

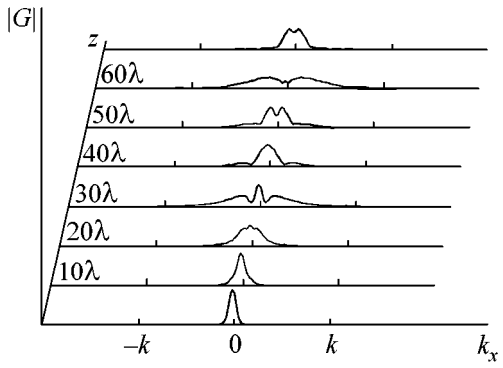


**Fig. 1.** Dynamics of the spatial spectrum for radiation in a nonlinear medium.

ceptibility; and $c$ is the speed of light in vacuum. In deriving Eq. (1), the generation of new optical harmonics was not taken into account.

To demonstrate the spectral method of self-focusing analysis, we restrict ourselves to the two-dimensional linearly polarized TE beams. In this case, Eq. (1) takes the form [1]

$$\Delta E + k^2 E + \chi |E|^2 E = 0, \tag{2}$$

where $E$ is the complex amplitude of a field polarized along the $y$ axis, $\Delta = \partial^2/\partial z^2 + \partial^2/\partial x^2$ is the two-dimensional Laplacian, $k = \sqrt{\epsilon} k_0$, and $\chi = 12\pi(\omega^2/c^2)\chi^{1111}$.

Choosing the $z$ axis as the propagation direction [in the numerical calculations, the two-dimensional field $E(x, z)$ is assumed to be symmetric about this axis], let us recast Eq. (2) for the spatial spectrum $G(k_x, z) = \int_{-\infty}^{\infty} E(x, z)\exp(-ik_x x)dx$ as

$$\frac{\partial^2 G}{\partial z^2} + (k^2 - k_x^2)G + \frac{\chi}{4\pi^2}\iint G^*(\alpha - k_x)G(\alpha - \beta)G(\beta)d\alpha d\beta = 0. \tag{3}$$

The linearized Eq. (3) has the solution

$$G = C_1(k_x)e^{i\sqrt{k^2 - k_x^2}z} + C_2(k_x)e^{-i\sqrt{k^2 - k_x^2}z}, \tag{4}$$

where the first and second terms correspond to radiation propagation in the positive and negative directions of the $z$ axis, respectively. The linear diffraction of a unidirectional wave (i.e., $C_2 = 0$) is described by the equation

$$\partial G/\partial z - i\sqrt{k^2 - k_x^2}G = 0. \tag{5}$$

Evidently, the solution of reduced Eq. (5) is simultaneously a partial solution of linearized Eq. (3). Physically, the reduction of linearized Eq. (3), i.e., transition to Eq. (5) containing a lower order $z$ derivative, is carried out with the aim of analyzing the diffraction of a unidirectional wave.

Let us generalize Eq. (5) to the nonlinear medium. The reduced nonlinear equation is sought in the form

$$\partial G/\partial z - i\sqrt{k^2 - k_x^2}G + \chi N(G) = 0, \tag{6}$$

where $N(G)$ is an unknown nonlinear operator. It will be found from the requirement that the solution of Eq. (6) be simultaneously a solution of nonreduced spectral Eq. (3). Differentiating Eq. (6) with respect to $z$ and expressing $\partial G/\partial z$ through $G$ from the same equation, one gets

$$\frac{\partial}{\partial z}\left(\frac{\partial G}{\partial z} - i\sqrt{k^2 - k_x^2}G + \chi N(G)\right) = \frac{\partial^2 G}{\partial z^2} + (k^2 - k_x^2)G + \chi\left(i\sqrt{k^2 - k_x^2}N(G) + \frac{\partial}{\partial z}N(G)\right) = 0. \tag{7}$$

Comparing (7) and (3), one obtains the following relationship for the $N(G)$ operator:

$$i\sqrt{k^2 - k_x^2}N(G) + \frac{\partial}{\partial z}N(G) = \frac{1}{4\pi^2} \times \int_{-\infty}^{\infty}\int_{-\infty}^{\infty} G^*(\alpha - k_x)G(\alpha - \beta)G(\beta)d\alpha d\beta. \tag{8}$$

Let us seek $N(G)$ in the form

$$N(G) = \int_{-\infty}^{\infty}\int_{-\infty}^{\infty} \varphi(k_x, \alpha, \beta)G^*(\alpha - k_x) \times G(\alpha - \beta)G(\beta)d\alpha d\beta, \tag{9}$$

where $\varphi(k_x, \alpha, \beta)$ is an unknown function. Then, using the fact that the relationships

$$\frac{\partial G(\alpha - \beta, z)}{\partial z} \approx i\sqrt{k^2 - (\alpha - \beta)^2}G(\alpha - \beta, z),$$
$$\frac{\partial G(\beta, z)}{\partial z} \approx i\sqrt{k^2 - \beta^2}G(\beta, z), \tag{10}$$
$$\frac{\partial G^*(\alpha - k_x, z)}{\partial z} \approx -i\left(\sqrt{k^2 - (\alpha - k_x)^2}\right)^* G^*(\alpha - k_x, z)$$

hold to higher order small terms, it is straightforward to obtain from Eqs. (8) and (9)

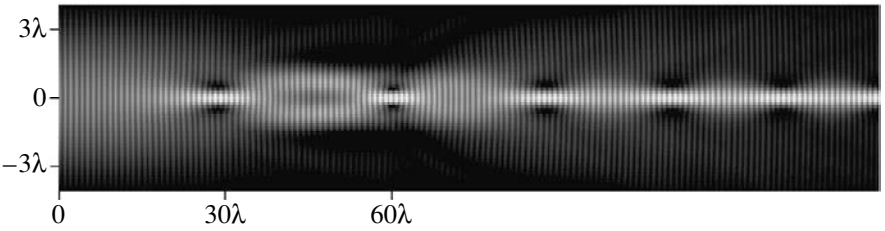


**Fig. 2.** Snapshot of self-focusing optical beam.

$$\varphi(k_x, \alpha, \beta) = -\frac{i}{4\pi}\frac{1}{\sqrt{k^2 - k_x^2} - \left(\sqrt{k^2 - (k_x - \alpha)^2}\right)^* + \sqrt{k^2 - (\alpha - \beta)^2} + \sqrt{k^2 - \beta^2}}. \quad (11)$$

Therefore, the reduced equation for the dynamics of the spatial spectrum of a unidirectional optical wave in a nonlinear medium takes the form

$$\frac{\partial G}{\partial z} - i\sqrt{k^2 - k_x^2}\,G = i\frac{\chi}{4\pi^2}\int_{-\infty}^{\infty}\int_{-\infty}^{\infty}\frac{G^*(\alpha - k_x, z)G(\alpha - \beta)G(\beta)\,d\alpha\,d\beta}{\sqrt{k^2 - k_x^2} - \left(\sqrt{k^2 - (k_x - \alpha)^2}\right)^* + \sqrt{k^2 - (\alpha - \beta)^2} + \sqrt{k^2 - \beta^2}}. \quad (12)$$

Applying manipulations (7)–(11) to this equation, one arrives at nonreduced Eq. (3) accurate to the terms fifth order in $G$ [because of the approximation (10)]. However, this accuracy is quite sufficient, because Eqs. (2) and (3) are derived from the outset with the same accuracy [1].

Eq. (12) can also be used to obtain a nonlinear reduced equation for the field,

$$E(x, z) = \frac{1}{2\pi}\int_{-\infty}^{\infty} G(k_x, z)\exp(ik_x z)\,dk_x.$$

However, it is more complicated than Eq. (12) and, even being linearized, remains an integrodifferential equation [5].

One of our numerical results is presented in Fig. 1, where the dynamics of the spatial spectrum is illustrated for a beam having Gaussian shape $E(x, 0) = E_0\exp(-(x/6\lambda)^2)$. At the input of a medium the maximum nonlinear component of the refractive index was $\chi|E_0|^2/2k^2 = 0.02$. One can see in Fig. 1 that the spectrum changes in a quasi-periodic manner. At a distance of approximately 30 wavelengths, its width becomes maximum and comparable with the wave number. Such an ultrabroadened spatial spectrum (this term is employed by analogy with the term "spectrum ultrabroadening" for a pulse with a spectral width comparable to the mean frequency [6]) contains spatial harmonics with frequencies exceeding the wave number. The second term in Eq. (12) becomes real for these harmonics. Hence, they correspond to the fields exponentially decreasing along $z$ and analogous to the fields appearing upon total internal reflection. One can see that if the second term in Eq. (12) is real then the corresponding components in the spectrum of the direct wave decrease, so that the back wave should appear in a transparent medium. Inasmuch as the energy loss due to the exponentially decaying field components of the radiation in the positive direction of the $z$ axis was small (less than 5%) in our numerical experiment, the influence of the back wave on the self-focusing of the direct wave was ignored in this work.

Figure 2 is a snapshot of the self-focusing beam field obtained by inverse transformation of the calculated spectrum dynamics. To make the photograph more pictorial, the transverse and longitudinal scales are different in Fig. 2. The quasi-periodicity of the spatial spectrum corresponds to the quasi-periodicity of the beam cross section. In the foci, the spatial spectrum acquires high-frequency components that are responsible for the radiation self-reflection. The field dynamics in Fig. 2 is shown for larger distances than in Fig. 1. It demonstrates not only the oscillatory character of changing the cross-sectional field structure but also the gradual damping of these oscillations and the formation of a quasi-stationary beam with a cross section close to the wavelength.

In summary, a new (spectral) method is suggested in this work for an analysis of nonparaxial self-focusing. This method is more convenient than the field method. It is tested by two-dimensional self-focusing, which is

not catastrophic in the paraxial approximation. Nevertheless, it is clear from above that radiation self-reflection would be the fundamental cause for field limitation in foci in the case of collapsing three-dimensional paraxial self-focusing as well.

## REFERENCES

1. S. V. Vlasov and V. I. Talanov, *Self-Focusing of Waves* (Inst. Prikl. Fiz. Ros. Akad. Nauk, Nizhni Novgorod, 1997).
2. V. E. Semenov, N. N. Rozanov, and N. V. Vysotina, Zh. Éksp. Teor. Fiz. **116**, 458 (1999) [JETP **89**, 243 (1999)].
3. S. Chi and Q. Guo, Opt. Lett. **20**, 1598 (1995).
4. M. D. Felt and J. A. Fleck, J. Opt. Soc. Am. B **5**, 633 (1988).
5. L. Fishman and J. J. McCoy, J. Math. Phys. **25**, 285 (1984).
6. V. G. Bespalov, S. A. Kozlov, A. N. Sutyagin, and Yu. A. Shpolyanskiĭ, Opt. Zh. **65**, 85 (1998).

*Translated by V. Sakun*

JETP Letters, Vol. 71, No. 11, 2000, pp. 457–459. Translated from Pis'ma v Zhurnal Éksperimental'noĭ i Teoreticheskoĭ Fiziki, Vol. 71, No. 11, 2000, pp. 671–674.


# Simultaneous Intercalation of Cesium and Potassium Atoms into a Two-Dimensional Graphite Film on Ir(111)

**N. R. Gall', E. V. Rut'kov, A. Ya. Tontegode, and Yu. N. Tsarev**

*Ioffe Physicotechnical Institute, Russian Academy of Sciences, Politekhnicheskaya ul. 26, St. Petersburg, 194021 Russia*

*e-mail: gall@ms.ioffe.rssi.ru*

Received April 25, 2000

The process of simultaneous intercalation of atoms differing in nature, namely, cesium and potassium, into a two-dimensional graphite film on a metal is studied. It is shown that, on being adsorbed simultaneously at room temperature, atoms of both sorts spontaneously penetrate into the space between the graphite film and the metal surface in approximately equal concentrations and remain there on heating up to graphite layer destruction temperatures (~ 2000 K). Upon the thermal destruction of the layer, potassium atoms escape first and cesium atoms escape thereafter. A physical description of the processes is developed. © *2000 MAIK "Nauka/Interperiodica".*

PACS numbers: 61.46.+w; 68.35.Bs

Considerable interest has been shown recently in the structure and properties of carbon single-wall nanotubes [1–3], whose mechanical and electrical properties are useful and promising. In many respects, the structure of two-dimensional graphite films (2DGFs) on metal surfaces is close to the structure of these remarkable systems. In fact, a 2DGF represents the lateral surface of a single-wall nanotube, but such a film is significantly easier to investigate.

We first observed intercalation in two-dimensional graphite films on metals in 1981 [4] and described it in detail in our reviews [5, 6]. It was found that 2DGFs are formed both on the surface of many metals that give no bulk carbides (Pt, Ni, Re, Ir, Ru, Rh, and Pd) and on bulk carbides of *d*-metals (Mo, Ta, Nb, Ti, Zr, and Hf) without commensurability with the substrate, which exists only for the Ni(111) face. These results are explained by the extremely high adsorption and chemical inertness of the graphite layer, which is bound to the substrate by only weak van der Waals forces and behaves like a two-dimensional crystal [7]. However, the carbon atoms inside the layer are bound very strongly and the film itself has the same atomic structure as a layer in a graphite single crystal. Intercalation in this case is spontaneous penetration of foreign particles (atoms [4–6] or fullerene $C_{60}$ molecules [8]) adsorbed on a 2DGF under the film. The film itself only moves aside from the metal surface, remaining virtually unchanged, just as graphite layers move apart upon intercalation into bulk graphite [9].

In the case of bulk intercalation compounds, a variety of most interesting properties (e.g., superconductivity etc.) are exhibited only when atoms of different nature penetrate into graphite interlayer spaces [10]. It was of interest to understand whether such simultaneous intercalation is possible in the case of two-dimensional graphite films on metals.

The experiments were performed in an ultra-high-vacuum ($P < 10^{-10}$ torr) high-resolution Auger electron spectrometer with a prism energy analyzer and in an ultra-high-vacuum static mass spectrometer [12]. The chemical state of the surface carbon (surface or bulk carbide, graphite, amorphous layer, diamond, etc.) was determined by high-resolution Auger electron spectroscopy ($\Delta E/E < 0.1\%$), and thermodesorption spectroscopy was used in the "ion burst" version [4, 12] for measuring the work function.

Iridium strips ($40 \times 1 \times 0.02$) mm warmed up by an alternating current were used as samples. The samples were cleaned by annealing for several hours at $T = 2200$ K under ultra-high vacuum, after which only iridium Auger peaks were observed on the surface. The strip surface texture corresponded to the (111) face by more than 99.5%, and the surface was uniform in work function. The temperature of the samples was measured by a micropyrometer. The temperature uniformity of the strips was better than $\Delta T \sim 10$ K.

Two-dimensional graphite films were produced by annealing a strip heated to 1700 K in benzene vapor ($P_{C_6H_6} \sim 10^{-7}$ torr). The $C_6H_6$ molecules were decomposed on a heated iridium surface, hydrogen was desorbed, and carbon was built in two-dimensional graphite islands. These islands grew, coalesced, and formed a continuous film [6]. The two-dimensionality of the film was obtained automatically, because the benzene molecules did not dissociate on the valence-saturated graphite surface and the supply of carbon into the adsorbed layer was terminated. The work function of the 2DGF surface was 4.45 eV, which is characteristic

0021-3640/00/7111-0457$20.00 

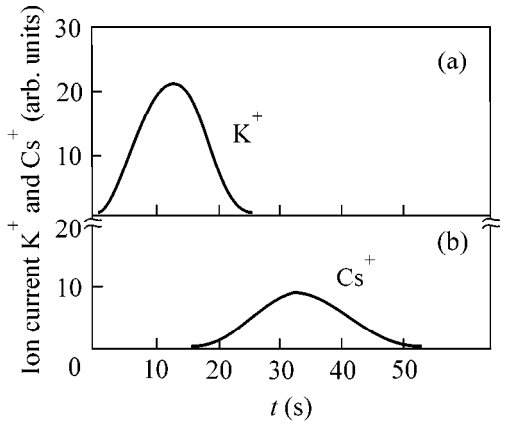


**Fig. 1.** Thermodesorption spectra (γ-phase) of (a) potassium and (b) cesium ions after their simultaneous sputtering onto a 2DGF on iridium at 300 K with equal fluxes of $\sim 4 \times 10^{11}$ cm$^{-2}$ c$^{-1}$ for 100 s. The spectra were recorded in the isothermal regime after the temperature was abruptly raised to 2100 K.

of the graphite basal plane [13]. The surface was uniform in work function.

We showed that, when intercalated separately, atoms with low ionization potentials (Cs, K, Na,…) intercalate into a 2DGF in a virtually similar way: at room temperature the flux of adsorbed atoms is divided into two approximately equal parts. One-half of the atoms penetrates under the layer and is accumulated there in the intercalated state (thermodesorption γ-phase), and the second half remains adsorbed on the outer film surface (α-phase). The limiting concentrations of electropositive atoms in both phases are on the order of one monolayer, $\sim 4 \times 10^{14}$ cm$^{-12}$, for both Cs and K. The heating of such a system leads to sequential thermodesorption of atoms: atoms of the α-phase fully leave the surface at $T \sim 700$–800 K. Conversely, the intercalated atoms (γ-phase) turn out to be immured under the graphite layer, thus preventing thermodesorption, and reside under it up to record high temperatures of ~ 2000 K and up [2, 3]. These atoms are desorbed only upon thermal destruction of graphite islands, which proceeds from their edges.

In the experiment, cesium and potassium atoms were simultaneously deposited onto a two-dimensional graphite film on iridium at 300 K with constant and equal fluxes of $\sim 4 \times 10^{11}$ cm$^{-2}$ c$^{-1}$ for 100 s. Next, an ion burst was initiated; that is, the desorbing $K^+$ and $Cs^+$ ions were measured. In our experiments, both these substances were desorbed only as positive ions formed through the surface ionization mechanism [14]. In this case, the strip temperature was abruptly raised to 2100 K and only the γ-phase was measured, that is, the atoms residing between the graphite layer and the metal surface. The experiment was successively repeated two times. Potassium and cesium were measured by mass spectrometry in the first and second cases, respectively (Fig. 1).

One can see that both elements are present in the thermodesorption spectrum in approximately equal amounts: $N_K \sim N_{Cs} \sim 1 \times 10^{13}$ cm$^{-2}$. This indicates that potassium and cesium atoms were simultaneously intercalated into the 2DGF. The delay of the cesium escape relative to the onset of the potassium escape upon the destruction of the graphite layer also deserves attention.

The accumulation of potassium and cesium in the intercalated state in almost equal concentrations is, in our opinion, due to the absence of competition between these atoms in the process of intercalation. This is not surprising, considering the closeness of the chemical and adsorption properties of both elements.

The delay of the desorption of cesium compared to potassium is of greater interest (Fig. 1). In all likelihood, the size of particles in the intercalated state plays a leading part in the observed effect. Both potassium and cesium occur on the surface in the ionized state, so that their ionic diameters should be compared. It is known that $d_{Cs^+} > d_{K^+}$, and the intercalated 2DGF at high temperatures may be conceived as a rigid mona-

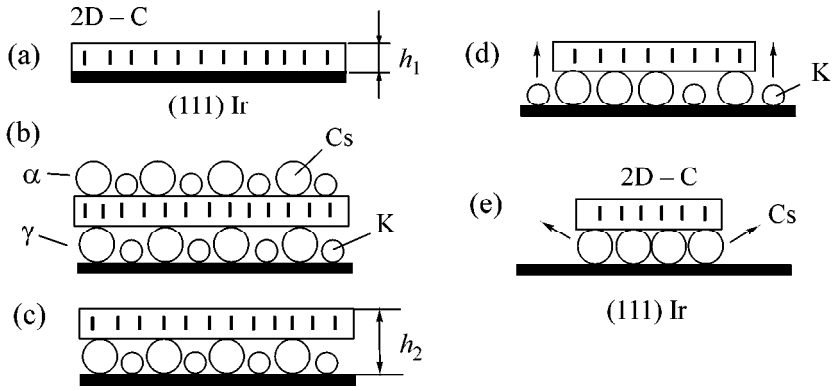


**Fig. 2.** Simplified schematic diagram of the processes of simultaneous intercalation of the Cs and K atoms into a 2DGF on Ir(111) followed by their thermal removal.

tomic carbon plate with the graphite structure, "lying" on the atoms of larger size, that is, on Cs. Therefore, escape from under the graphite layer is not equivalent for K and Cs: the smaller atoms escape more easily. Within this picture of simultaneous intercalation in a 2DGF, the process of thermal removal of potassium and cesium can be schematically depicted as shown in Fig. 2:

(a) 2DGF on iridium in the absence of intercalation is bound to the metal by weak van der Waals forces; in this case, $h_1 = 3.35$ Å [7, 15, 16].

(b) Simultaneous adsorption of potassium and cesium at 300 K results in the filling of both α- and γ-phases.

(c) Heating to 800 K removes atoms adsorbed over the graphite layer (α-phase). The 2DGF is separated from the metal surface by a distance of $h_2 \sim 6$–7 Å, which is necessary for the $Cs^+$ ions to be placed between the film and the metal surface.

(d) Heating to 2100 K leads to the onset of the destruction of graphite islands and removal of potassium. After desorption of potassium, cesium is "condensed" under the graphite islands.

(e) Further destruction of graphite islands proceeds, and cesium atoms are desorbed.

Thus, it is shown that the potassium and cesium atoms intercalate into a 2DGF on iridium(111) to accumulate between the film and the metal surface in approximately equal concentrations. Upon thermal destruction of the film ($T \sim 2100$ K), potassium escapes first from under the film and cesium escapes next. Note that the new effect of simultaneous intercalation into 2DGF on metals found in this work is important, because it significantly increases the number of intercalated systems and allows the systems with promising physical and chemical properties to be fabricated.

This work was supported by the Program of the Ministry of Science of the Russian Federation Physics of Solid-State Nanostructures, project no. 99-2039.

## REFERENCES

1. *Essentials of Carbon–Carbon Composites*, Ed. by C. R. Thomas (Royal Soc. of Chemistry, Cambridge, 1993).
2. *Physics and Chemistry of the Fullerenes*, Ed. by K. Prassides (Kluwer Academic, Dordrecht, 1994).
3. S. Iijima, Nature (London) **354**, 56 (1991).
4. E. V. Rut'kov and A. Ya. Tontegode, Pis'ma Zh. Tekh. Fiz. **7**, 1122 (1981) [Sov. Tech. Phys. Lett. **7**, 480 (1981)].
5. A. Ya. Tontegode and E. V. Rut'kov, Usp. Fiz. Nauk **163**, 57 (1993) [Phys.-Usp. **36**, 1053 (1993)].
6. N. R. Gall, E. V. Rut'kov, and A. Ya. Tontegode, Int. J. Mod. Phys. B **11**, 1865 (1997).
7. A. Ya. Tontegode, Prog. Surf. Sci. **38**, 201 (1991).
8. E. V. Rut'kov, A. Ya. Tontegode, and M. M. Usufov, Phys. Rev. Lett. **74**, 758 (1995).
9. M. S. Dresselhaus and G. Dresselhaus, Adv. Phys. **30**, 139 (1981).
10. *Proceedings of the 5th International Symposium on Graphite Intercalation Compounds, Berlin, 1989*, Ed. by K. Luders and R. Schollhorn; Synth. Met. **34**, 68 (1989/1990).
11. N. R. Gall, S. N. Mikhailov, E. V. Rut'kov, and A. Ya. Tontegode, Surf. Sci. **191**, 185 (1987).
12. E. V. Rut'kov and A. Ya. Tontegode, Surf. Sci. **161**, 373 (1985).
13. V. S. Fomenko, *Emissional Properties of Materials: Reference Book* (Naukova Dumka, Kiev, 1981).
14. E. Ya. Zandberg and N. I. Ionov, *Surface Ionization*, Israel Program for Scientific Translations (Jerusalem, 1971).
15. Hu Zi-Pu, D. F. Ogletree, M. A. Van-Hove, and G. A. Somorjai, Surf. Sci. **180**, 433 (1987).
16. R. Rossei, M. De Crescenzi, F. Sett, *et al.*, Phys. Rev. B **28**, 1161 (1983).

*Translated by A. Bagatur'yants*

JETP Letters, Vol. 71, No. 11, 2000, pp. 460–464. Translated from Pis'ma v Zhurnal Éksperimental'noĭ i Teoreticheskoĭ Fiziki, Vol. 71, No. 11, 2000, pp. 675–681.


# Two-Sublattice Ordering in Titanium Monoxide

**A. A. Valeeva, A. A. Rempel', and A. I. Gusev**

*Institute of Solid-State Chemistry, Ural Division, Russian Academy of Sciences, Pervomaiskaya ul. 91, Yekaterinburg, 620219 Russia*

*e-mail: gusev@ihim.uran.ru and/or valeeva@ihim.uran.ru*

Received April 27, 2000

The disordered and ordered structures of nonstoichiometric titanium monoxide $Ti_xO_z \equiv TiO_y$ ($y = z/x$) containing structural vacancies simultaneously in the nonmetallic and metallic sublattices were studied. In the stoichiometry range from $TiO_{0.9}$ to $TiO_{1.1}$, an ordered monoclinic phase [space group $C2/m$ ($A12m/1$)] of the $Ti_5O_5$ type is formed in the $TiO_y$ monoxide at temperatures below 1300 K. The disorder–order $TiO_y$–$Ti_5O_5$ phase-transition channel involves Lifshitz $\{\mathbf{k}_{10}\}$ and non-Lifshitz $\{\mathbf{k}_4\}$ and $\{\mathbf{k}_{11}\}$ star rays. The ordering proceeds as a first-order phase transition with a decrease in the volume of the basal cubic lattice. The titanium and oxygen distribution functions in the metallic and nonmetallic sublattices of titanium monoxide are calculated. The domain of allowed values is determined for the long-range order parameter. © *2000 MAIK "Nauka/Interperiodica".*

PACS numbers: 61.50.Ks; 61.66.Fn; 61.50.Nw

Nonstoichiometric titanium monoxide $TiO_y$ of basal structure $B1$ belongs to a group of strongly nonstoichiometric interstitial compounds [1, 2]. It is homogeneous over a wide range from $TiO_{0.80}$ to $TiO_{1.25}$ and is unique even among highly nonstoichiometric compounds because of a diversity of structural vacancies (unoccupied crystal sites) in its nonmetallic and metallic sublattices. To correctly describe the real structure of titanium monoxide, its composition should be formulated with allowance made for the structural vacancies in each of the sublattices, i.e., as $Ti_xO_z \equiv TiO_y$ or $Ti_x\blacksquare_{1-x}O_z\square_{1-z} \equiv TiO_y$, where $y = z/x$ and □ and ■ stand for the structural vacancies in the nonmetallic (oxygen) and metallic (titanium) sublattices, respectively. For instance, titanium monoxide of formal stoichiometry $TiO_{1.0}$ contains ~15–16 at. % vacancies in both titanium and oxygen sublattices and, hence, its real composition is $\sim Ti_{0.84–0.85}O_{0.84–0.85}$ [3]. In the disordered state, the atoms and structural vacancies are randomly distributed over the sites of relevant sublattices, although the cubic symmetry of each sublattice is retained, because the probability of finding an atom in a certain site is identical for all sites of the corresponding sublattice and equal to the relative content of the occupied sites in the sublattice, i.e., is equal to $x$ for the titanium sublattice and $z$ for the oxygen sublattice.

It is known that, under certain circumstances, the structural vacancies may induce ordering in strongly nonstoichiometric interstitial compounds [4].

Depending on the oxygen content and heat treatment regime, the atomic and vacancy distributions in the $TiO_y$ lattice may be either disordered or ordered. The disordered state is thermodynamically stable at $T >$ 1600 K, while at temperatures below 1500 K, several ordered phases of different types and different symmetry form in different concentration and temperature ranges [1, 4]. However, the disordered state of titanium monoxide $TiO_y$ can easily be stabilized by quenching from $T >$ 1600 K, whereupon it can exist as a metastable state at room temperature as long as one likes.

Up to now, the studies of the ordered phases of titanium monoxide $TiO_y$ were restricted to crystal structure determination [5–9]. At the same time, diversified and detailed information about the disorder–order transition and the corresponding long-range order parameters can be gained from an analysis of the symmetry changes occurring in the course of the ordering process. With this in mind, the ordering in the nonmetallic and metallic sublattices of cubic titanium monoxide is examined in this work, and the symmetry analysis is carried out for the resulting monoclinic superstructure.

Nonstoichiometric samples of cubic titanium monoxide $TiO_y$ with different oxygen contents were synthesized by the solid-phase sintering of powder mixtures of metallic titanium and titanium dioxide $TiO_2$ in vacuum (0.0013 Pa) at temperature 1770 K for 70 h. The surface color of the synthesized samples changed from yellowish silver for $TiO_{0.7–0.8}$ oxides to deep golden yellow for $TiO_{1.2–1.3}$ oxides. Near-equiatomic titanium monoxide $TiO_{1.03–1.08}$ assumed the characteristic golden yellow color. The synthesized samples were subjected to annealing followed by quenching in evacuated quartz tubes. An increase in the oxygen content in the quenched disordered $TiO_y$ monoxide brought about a decrease in the $a_{B1}$ period, in compliance with the experimental data [3, 10].

To determine the vacancy concentrations in the metallic and nonmetallic sublattices of $TiO_y$ monoxide,

the true density ρ of the quenched samples was measured by a pycnometer. The site occupancy for the titanium atoms in the metallic sublattice was determined by the formula [1]

$$x = \rho_{exp} V c_{Ti} / N A_{Ti} g, \quad (1)$$

where $\rho_{exp}$ is the density measured by a pycnometer; $V = a_{B1}^3$ is the unit-cell volume; $c_{Ti}$ is the titanium mass fraction in the sample; $N = 4$ is the number of formula units in the unit cell of $TiO_y$ monoxide; and $g = 1.66 \times 10^{-27}$ kg is the atomic mass unit. The relative vacancy content in the titanium sublattice is $c_{\blacksquare} = 1 - x$. The site occupancy for the oxygen atoms in the nonmetallic sublattice is $z = xy$, and the relative content of structural vacancies in the oxygen sublattice is $c_{\square} = 1 - z$.

To prepare the ordered state, the quenched samples of the disordered titanium monoxide were annealed in evacuated quartz tubes at a temperature of 1330 K for 3 h, then slowly cooled from 1330 to 300 K at a rate of 10 K/h. The diffraction studies were carried out on a Siemens D-500 autodiffractometer with Cu$K\alpha_{1,2}$ radiation in the Bragg–Brentano geometry. The X-ray measurements were performed in the step-by-step scan regime with $\Delta(2\theta) = 0.025°$ in the $2\theta$ range from 10° to 160°; the exposure time was 13 s for every point.

A detailed X-ray study of the annealed $TiO_{1.087}$ monoxide revealed a set of reflections with intensities no less than 5% of the intensity of structural reflections, in addition to the basal cubic reflections of the *B*1 structure. Figure 1 shows the typical X-ray diffraction pattern of the annealed ordered $TiO_{1.087}$ monoxides. The appearance of weak reflections is evidence for the formation of a superstructure in the annealed nonstoichiometric titanium monoxide.

The literature data on the ordering in $TiO_y$ are incomplete and contradictory. It is known that the monoclinic superstructure occurs in the $TiO_{1.0}$ ($Ti_{0.84}O_{0.84}$ or $Ti_{0.83}O_{0.83}$) monoxide below 1200–1250 K [5–7], while the ordered cubic phase can arise in the temperature range from 1250 to 1500 K [7]. However, according to [11], only a single ordered monoclinic phase (space group *C*2/*m* or *A*2/*m*) exists in the low-temperature annealed titanium monoxide with oxygen content from 36 to 50 at. % ($TiO_{0.56}$–$TiO_{1.00}$). In $TiO_y$ with $y \geq 1.2$, the ordered orthorhombic and tetragonal phases were found upon annealing at a temperature below 1090 K [7].

An analysis of the superstructural reflections in the X-ray pattern of the annealed $TiO_{1.087}$ oxide (Fig. 1) showed that the first Brillouin zone of the fcc lattice involved five nonequivalent vectors responsible for the disorder–order structural transition channel (Fig. 2): the $\mathbf{k}_{10}^{(1)} = (\mathbf{b}_1 + \mathbf{b}_2)/2 = (0\,0\,1)$ ray of the Lifshitz $\{\mathbf{k}_{10}\}$ star; two $\mathbf{k}_4^{(5)} = \mu_4(\mathbf{b}_1 + 2\mathbf{b}_2 + \mathbf{b}_3) = (2/3\ 0\ 2/3)$ and $\mathbf{k}_4^{(6)} = -\mathbf{k}_4^{(5)}$ rays of the non-Lifshitz $\{\mathbf{k}_4\}$ star with the current parameter $\mu_4 = 1/3$; and two $\mathbf{k}_1^{(7)} = \mu_1^{(1)}(\mathbf{b}_2 + \mathbf{b}_3) - \mu_1^{(2)}(\mathbf{b}_1 + \mathbf{b}_2) = (2/3\ 0\ -1/3)$ and $\mathbf{k}_1^{(8)} = -\mathbf{k}_1^{(7)}$ rays of the non-Lifshitz $\{\mathbf{k}_1\}$ star with the current parameters $\mu_1^{(1)} = 1/3$ and $\mu_1^{(2)} = 1/6$ (the numbering of the wave-vector stars $\{\mathbf{k}_s\}$ and the rays $\mathbf{k}_s^{(j)}$ of these stars in the first Brillouin zone of fcc crystals is given in [4, 12]).

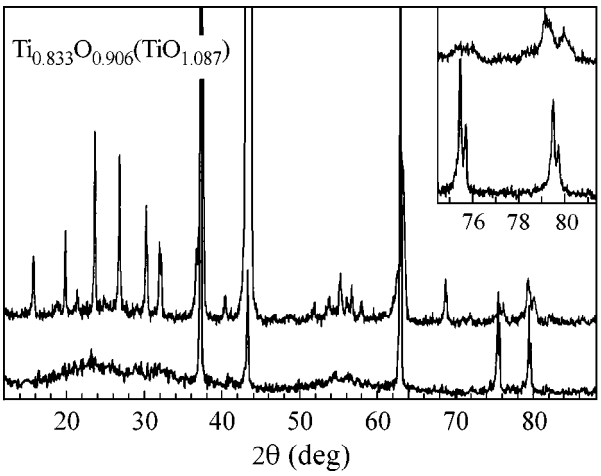


**Fig. 1.** X-ray diffraction patterns of the quenched disordered and the annealed ordered titanium monoxide $Ti_{0.833}O_{0.906}$ ($TiO_{1.087}$). Splitting of the diffraction reflections into $\alpha_1$ and $\alpha_2$ doublets observed for the (311)*B*1 and (222)*B*1 lines and other reflections of the basal *B*1 structure (inset) is evidence for a high degree of homogeneity of the quenched disordered $TiO_{1.087}$ monoxide.

The distribution of atoms of sort ν in the ordered crystal is described by the distribution function $n_\nu(\mathbf{r})$ of symmetry corresponding to the ordered lattice. The distribution function $n_\nu(\mathbf{r})$ is the probability of an atom of sort ν being found at crystal site **r**. In the disordered $Ti_xO_z$ monoxide, the probabilities $n_{Ti}(\mathbf{r})$ and $n_O(\mathbf{r})$ coincide with the fractions of sites occupied, respectively, by the titanium and oxygen atoms in the corresponding sublattices; i.e., $n_{Ti}(\mathbf{r}) = x$ and $n_O(\mathbf{r}) = z$.

After the disorder–order transition, the uniform atomic distribution over the sites in the disordered compound becomes spatially periodically modulated; i.e., the probability $n_\nu(\mathbf{r})$ deviates from its value corresponding to the disordered distribution. This modulation can be imagined as a superposition of several plane concentration waves whose wave vectors coincide with the superstructure vectors responsible for the disorder–order transition channel [13, 14]. For each of the wave-vector stars $\{\mathbf{k}_s\}$, there is a long-range order parameter $\eta_s$. Therefore, the atomic distribution function can be found for any superstructure if the transition channel is known.

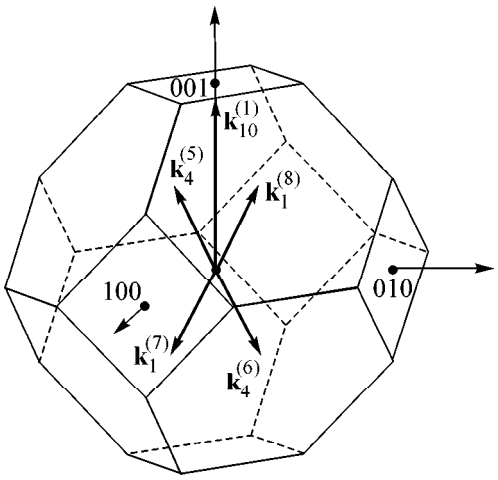


**Fig. 2.** The disorder–order structural phase transition $TiO_y$(space group $Fm\bar{3}m$)–$Ti_5O_5$(space group $C2/m$) channel: the positions of nonequivalent superstructural vectors in the first Brillouin zone of the fcc lattice of a disordered crystal.

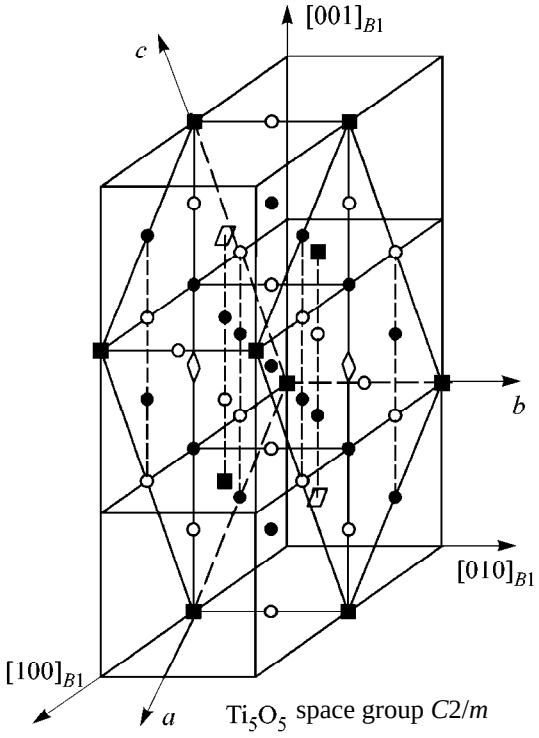


**Fig. 3.** Ideal monoclinic [space group $C2/m$ ($A12/m1$)] unit cell of the ordered $Ti_5O_5$ phase in the lattice with structure $B1$: ● is the Ti atom; ○ is the O atom; ■ is the structural vacancy in the titanium sublattice; and □ is the structural vacancy in the oxygen sublattice. For the disordered $Ti_{0.833}O_{0.833}$ ($TiO_{1.0}$) monoxide with basal lattice period $a_{B1}$ = 0.4174 nm, the parameters of an ideal undistorted unit cell of monoclinic superstructure are $a_m$ = 0.59029 nm, $b_m$ = 0.4174 nm, $c_m$ = 0.9333 nm, and $\beta$ = 108.43(5)°.

The calculations showed that the titanium distribution function in the superstructure of titanium monoxide $Ti_xO_z$ has the form

$$\begin{aligned} n_{\mathrm{Ti}}(x_\mathrm{I}, y_\mathrm{I}, z_\mathrm{I}) &= x - (\eta_{10}^{\mathrm{Ti}}/6)\cos 2\pi z_\mathrm{I} \\ &- (\eta_4^{\mathrm{Ti}}/3)\cos[4\pi(x_\mathrm{I} + z_\mathrm{I})/3] \\ &- (\eta_1^{\mathrm{Ti}}/3)\cos[2\pi(2x_\mathrm{I} - z_\mathrm{I})/3], \end{aligned} \quad (2)$$

while the oxygen distribution in the same superstructure is described by the function

$$\begin{aligned} n_{\mathrm{O}}(x_\mathrm{I}, y_\mathrm{I}, z_\mathrm{I}) &= z + (\eta_{10}^{\mathrm{O}}/6)\cos 2\pi z_\mathrm{I} \\ &- (\eta_4^{\mathrm{O}}/3)\cos[4\pi(x_\mathrm{I} + z_\mathrm{I})/3] \\ &+ (\eta_1^{\mathrm{O}}/3)\cos[2\pi(2x_\mathrm{I} - z_\mathrm{I})/3], \end{aligned} \quad (3)$$

where $x_\mathrm{I}$, $y_\mathrm{I}$, and $z_\mathrm{I}$ are the coordinates of site **r** in the ordered sublattice and $\eta_{10}$, $\eta_4$, and $\eta_1$ are the long-range order parameters.

The completely ordered state is achieved for titanium monoxide when all long-range order parameters become equal to unity for each sublattice; i.e., $\eta_{10} = \eta_4 = \eta_1 = 1$. It follows from distribution functions (2) and (3) that the relative titanium concentration in the corresponding metallic sublattice is $x = 5/6$, while the relative oxygen concentration in the nonmetallic sublattice is $z = 5/6$. Thus, the stoichiometry of the ideal superstructure can be formulated as $Ti_{5/6}O_{5/6}$ ($Ti_{0.83}O_{0.83}$) or $Ti_5O_5$ ($Ti_5\blacksquare_1O_5\square_1$).

If the distribution functions $n_{\mathrm{Ti}}(\mathbf{r})$ and $n_{\mathrm{O}}(\mathbf{r})$ and the reciprocal lattice translation vectors are known, one can construct the corresponding unit cell for the ideal ordered titanium monoxide $Ti_5O_5$ (Fig. 3). In the coordinates of basal structure $B1$, the primitive translation vectors of this superstructure are $a_m = \{1\ 0\ {-1}\}_{B1}$, $b_m = \{0\ 1\ 0\}_{B1}$, and $c_m = \{1\ 0\ 2\}_{B1}$. The unit cell is monoclinic; belongs to the space group $C2/m$; and contains two formula units $Ti_5O_5$, i.e., ten titanium atoms, ten oxygen atoms, two vacancies in the titanium sublattice, and two oxygen vacancies. Therefore, the metallic and nonmetallic sublattices of the ideal monoclinic $Ti_5O_5$ superstructure each contain ~16.7 at. % vacancies. This means that the vacancy content in the titanium and oxygen sublattices of the disordered titanium monoxide $TiO_{1.0}$ is also equal to 16.7 at. % rather than to 15–16 at. %, as was assumed by the authors of [3, 6].

Since the titanium $TiO_{1.087}$ ($Ti_{0.833}3O_{0.906}$) monoxide studied is compositionally different from the equiatomic $TiO_{1.0}$ ($Ti_{0.833}O_{0.833}$), the ratio of reflection intensities in the X-ray diffraction pattern of the ordered $TiO_{1.087}$ slightly differs from that in the X-ray pattern of the ideal monoclinic $Ti_5O_5$ superstructure.

It was shown in [4] that for the superstructure of the $M_{2t}X_{2t-1}(A_{2t-1}B)$ type, the dependence of the maximum value of the long-range order parameter on the

composition of the nonstoichiometric $MX_y$ compound (or the $A_yB_{1-y}$ solid solution) has the form

$$\eta^{\max}(y) = \begin{cases} 2t(1-y), & \text{if } y \geq ((2t-1)/2t), \\ 2ty/(2t-1), & \text{if } y < (2t-1)/2t. \end{cases} \quad (4)$$

The superstructure formed in $TiO_{0.9}$–$TiO_{1.1}$ is of the $Ti_5\blacksquare_1O_5\square_1$ type with $t = 3$. Accordingly, the long-range order parameters in the titanium and oxygen sublattices of the $TiO_{1.087}$ ($Ti_{0.833}O_{0.906}$) monoxide have the maximum values of 1.00 and 0.56, respectively.

The best agreement between the calculated diffraction spectrum of the ordered $TiO_{1.087}$ monoxide and the experimental X-ray diffraction pattern is achieved when the long-range order parameters are taken to be $\eta_{10}^{Ti} = \eta_4^{Ti} = \eta_1^{Ti} = 1.00$ and $\eta_{10}^{O} = \eta_4^{O} = \eta_1^{O} = 0.56$ for the titanium and oxygen sublattices, respectively. The remaining distinctions between the experimental and theoretical diffraction spectra are due to the presence of a disordered phase in, on the whole, ordered annealed titanium monoxide $TiO_{1.087}$.

Physically, the distribution function $n(\mathbf{r})$ is a probability and, hence, can take values between 0 and 1. The distribution functions (2) and (3) calculated for the titanium and oxygen atoms depend on the composition of the $TiO_y$ monoxide and on to which of the sublattices in the ordered structure the site $\mathbf{r}$ belongs. In the simplest case where the superstructure is described by a single long-range order parameter, the domain of allowed values of this parameter is bounded by the minimum (zero) value and the maximum value determined from Eq. (4). However, if there are several such parameters, additional limitations are placed on the distribution functions. The domain of allowed values of the long-range order parameters was determined by the calculation of the values the distribution functions $n_{Ti}(\mathbf{r})$ (2) and $n_O(\mathbf{r})$ (3) take at the sites of the titanium and oxygen sublattices.

The domain of allowed values of the order parameters in both sublattices of the monoclinic (space group $C2/m$) $Ti_5O_5$ ($Ti_{2t-1}\blacksquare_1O_{2t-1}\square_1$ with $t = 3$) superstructure formed in titanium monoxide $TiO_y \equiv Ti_xO_z$ (Fig. 3) is determined by the following set of inequalities:

$$\begin{aligned} -2m^{*(\mathrm{Ti,O})} &\leq \eta_{10}^{(\mathrm{Ti,O})} - 2\eta_4^{(\mathrm{Ti,O})} + 2\eta_1^{(\mathrm{Ti,O})} \leq m^{*(\mathrm{Ti,O})}, \\ -m^{*(\mathrm{Ti,O})}/2 &\leq \eta_{10}^{(\mathrm{Ti,O})} + \eta_4^{(\mathrm{Ti,O})} - \eta_1^{(\mathrm{Ti,O})} \leq m^{*(\mathrm{Ti,O})}, \\ -m^{*(\mathrm{Ti,O})} &\leq \eta_{10}^{(\mathrm{Ti,O})} + \eta_4^{(\mathrm{Ti,O})} + \eta_1^{(\mathrm{Ti,O})} \leq m^{*(\mathrm{Ti,O})}. \end{aligned} \quad (5)$$

In Eq. (5), $m^{*(\mathrm{Ti})} = 6(1-x)$ if $x \geq 5/6$, $m^{*(\mathrm{Ti})} = 6x/5$ if $x < 5/6$, $m^{*(\mathrm{O})} = 6(1-z)$ if $z \geq 5/6$, and $m^{*(\mathrm{O})} = 6z/5$ if $z < 5/6$. The polyhedron bounding the domain of allowed values of the order parameters in the monoclinic (space group $C2/m$) $Ti_5O_5$ superstructure (Fig. 4) has the same shape as that found in [13, 15] for the monoclinic (space group $C2/m$) and trigonal (space group $P3_1$) superstructures of the $M_6X_5$ type.

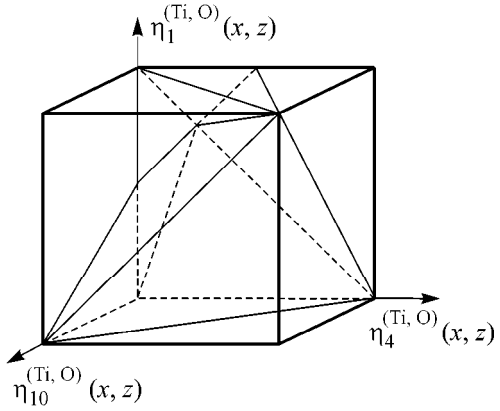


**Fig. 4.** Three-dimensional domain of allowed values of the long-range order parameters for the monoclinic (space group $C2/m$) ordered $Ti_5O_5$ structure.

The presence of the vectors of two non-Lifshitz $\{\mathbf{k}\}$ and $\{\mathbf{k}_1\}$ stars in the disorder–order $TiO_y$–$Ti_5O_5$ transition channel implies that the Landau criterion for second-order phase transitions is not fulfilled and that the formation of the monoclinic $Ti_5O_5$ superstructure in titanium monoxide $TiO_y$ is a first-order phase transition. The experimentally observed difference in the volumes $a_{B1}^3$ of basal lattices in the compositionally identical disordered and ordered $TiO_y$ monoxides confirms that the $TiO_y$ ordering is a first-order transition. The disordered $TiO_{1.087}$ monoxide has a period of $a_{B1} = 0.4174$ nm and, correspondingly, a volume of $72.72 \times 10^{-3}$ nm$^3$, while after ordering the basal lattice volume decreases to $72.23 \times 10^{-3}$ nm$^3$, which corresponds to a period of $a_{B1} = 0.4164$ nm.

In summary, the X-ray diffraction studies and the symmetry analysis of the ordering in the nonstoichiometric cubic titanium monoxide $TiO_y$ enabled one to determine the channel for, and the type of, the structural disorder–order phase transition $TiO_y$–$Ti_5O_5$ [space group $C2/m$ ($A12/m1$)] and calculate the distribution functions for the titanium and oxygen atoms in the crystal lattice of the monoclinic $Ti_5O_5$ superstructure. In essence, the ordering in titanium monoxide is the ordering in a four-component compound, because the titanium and oxygen atoms and the titanium and oxygen vacancies are physically and crystallographically nonequivalent. The resulting distribution functions may be used in the thermodynamic calculation of the ordering process in cubic titanium monoxide.

This work was supported by the Russian Foundation for Basic Research, project no. 98-03-32856a.

## REFERENCES


1. A. I. Gusev, *Physical Chemistry of Nonstoichiometric High-Melting Compounds* (Nauka, Moscow, 1991).
2. A. I. Gusev, Usp. Fiz. Nauk **170**, 3 (2000).
3. S. Andersson, B. Collen, U. Kuylenstierna, and A. Magneli, Acta Chem. Scand. **11**, 1641 (1957).
4. A. I. Gusev and A. A. Rempel', *Structural Phase Transitions in Nonstoichiometric Compounds* (Nauka, Moscow, 1988).
5. U. Kuylenstierna and A. Magneli, Acta Chem. Scand. **10**, 1195 (1956).
6. D. Watanabe, J. R. Castles, A. Jostsons, and A. S. Malin, Nature (London) **210**, 934 (1966).
7. E. Hilti, Naturwissenschaften **55**, 130 (1968).
8. E. Hilti and F. Laves, Naturwissenschaften **55**, 131 (1968).
9. D. Watanabe, O. Terasaki, A. Jostsons, and J. R. Castles, in *The Chemistry of Extended Defects in Non-Metallic Solids*, Ed. by L. Eyring and M. O. Keeffe (North-Holland, Amsterdam, 1970), p. 238.
10. M. D. Banus, T. B. Reed, and A. J. Strauss, Phys. Rev. B **5**, 2775 (1972).
11. B. V. Khaenko and É. T. Kachkovskaya, Poroshk. Metall. (Kiev), No. 6, 52 (1986).
12. O. V. Kovalev, *Irreducible Representations of Space Groups* (Naukova Dumka, Kiev, 1961; Gordon & Breach, New York, 1965).
13. A. A. Rempel', *Ordering Effects in Nonstoichiometric Interstitial Phases* (Nauka, Yekaterinburg, 1992).
14. A. I. Gusev and A. A. Rempel', Phys. Status Solidi A **135**, 15 (1993).
15. A. I. Gusev and A. A. Rempel', J. Phys. C: Solid State Phys. **20**, 5011 (1987).


*Translated by V. Sakun*

JETP Letters, Vol. 71, No. 11, 2000, pp. 465–468. Translated from Pis'ma v Zhurnal Éksperimental'noĭ i Teoreticheskoĭ Fiziki, Vol. 71, No. 11, 2000, pp. 682–686.


# $^{57}$Fe NMR Study of a Spatially Modulated Magnetic Structure in $BiFeO_3$

**A. V. Zalesskiĭ*, A. K. Zvezdin**, A. A. Frolov*, and A. A. Bush*****

** Shubnikov Institute of Crystallography, Russian Academy of Sciences, Leninskiĭ pr. 59, Moscow, 117333 Russia*
*e-mail: nmr@ns.crys.ras.ru*
*** Institute of General Physics, Russian Academy of Sciences, ul. Vavilova 38, Moscow, 117942 Russia*
**** Moscow State Institute of Radio Engineering, Electronics, and Automation (Technical University), pr. Vernadskogo 78, Moscow, 117454 Russia*

Received May 10, 2000

The $^{57}$Fe spin echo spectra were studied in local magnetic fields of a $BiFeO_3$ ferroelectric antiferromagnet over the temperature range 77–304 K. The line shape analysis confirmed the presence of a spatially modulated, incommensurate cycloidal spin structure in $BiFeO_3$ and allowed the actual spin distribution to be reproduced throughout the cycloid length. The distribution was found to be essentially anharmonic. The modulated structure is stable over the whole temperature range studied. The cycloid wave becomes more harmonic with temperature elevation. © *2000 MAIK "Nauka/Interperiodica".*

PACS numbers: 76.60.Lz; 75.25.+z

The $BiFeO_3$ compound belongs to the class of so-called ferroelectric ferromagnets, i.e., materials exhibiting both electric-dipole and magnetic-spin ordering. After the discovery of ferroelectric ferromagnets in 1960–1962, their properties were intensively studied in succeeding years (see, e.g., monograph [1], where the works published until 1980 are reviewed). It was established that $BiFeO_3$ has a rhombohedrally distorted perovskite-like structure (space group $R3c$) [2] with a bimolecular unit cell in which the $Fe^{3+}$ and $Bi^{3+}$ ions are so displaced along the threefold axis that the electric polarization becomes nonzero (according to [3], the corresponding Curie temperature $T_C \approx 1118$ K). The parameters of the rhombohedral unit cell of $BiFeO_3$ at room temperature are the following: $a = 3.96$ Å and $\alpha = 89°28'$; in the hexagonal system, $a_{hex} = 5.5876$ and $c_{hex} = 13.876$ Å [2]. According to the original neutron diffraction studies [4], BiFeO3 is an antiferromagnet with the *G*-type spin ordering below the Néel temperature $T_N \approx 653$ K. This implies that every magnetic $Fe^{3+}$ ion is surrounded by six neighboring $Fe^{3+}$ ions with spins antiparallel to the central ion spin. More recently, the magnetic structure of $BiFeO_3$ was studied using a high-precision high-resolution time-of-flight diffractometer [5]. From the splitting of magnetic diffraction peaks, the conclusion was drawn about the presence in $BiFeO_3$ of a magnetic cycloidal spiral with a large period $\lambda = 620 \pm 20$ Å that is incommensurate with the lattice parameter. According to [5], the magnetic moments of the $Fe^{3+}$ ions, while retaining local antiferromagnetic *G*-type mutual orientation, are turned in the plane perpendicular to the hexagonal basal plane along the propagation direction of the modulated wave. The wave vector **q** of such a cycloid is perpendicular to the threefold axis (*c*) and lies in the plane of spin rotation. According to [6], the cycloidal spiral persists up to $T_N$.

The possibility for the magnetic spiral (at first sight, unusual for weakly distorted perovskites) to appear was theoretically substantiated in [7, 8], where the phenomenological treatment of crystal structure symmetry suggested that the thermodynamic potential of $BiFeO_3$ can contain a Lifshitz-type invariant. It was found by the minimization of this potential that the spatially modulated spin structure, experimentally observed in [5], can occur in such systems. For the threefold axis to be retained in the $R3c$ group, the **q** vector must belong to the wave-vector star. Therefore, macroscopically, the magnetic structure of the $BiFeO_3$ crystal can be regarded as a superposition of the contributions from three pairs of physically equivalent rays, much as it occurs when crystal is divided into domains upon cooling below the Curie point.

A change in the angle $\theta$ between the antiferromagnetic vector **L** and the axis *c* along the cycloid propagation direction (*x*-axis) is given by [7]

$$\cos\theta(x) = sn\left(\pm\frac{4K(m)}{\lambda}x, m\right), \quad (1)$$

where $sn(x, m)$ is the elliptic Jacobi function, $m$ is its parameter, and $K(m)$ is the complete elliptic integral of the first kind. The period $\lambda$ of the spatially modulated wave is expressed through the energy parameters of the thermodynamic potential, the so-called exchange stiff-

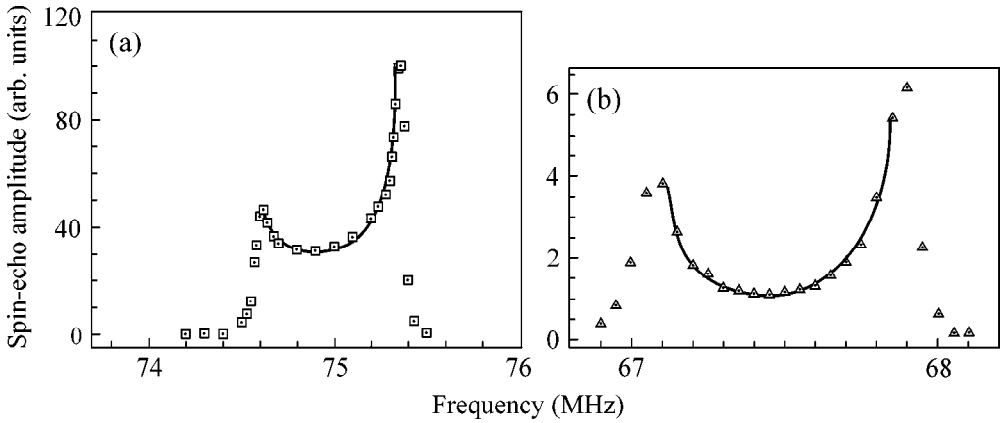


**Fig. 1.** The $^{57}$Fe spin echo spectra in $BiFeO_3$ at (a) 77 and (b) 304 K. The solid lines are the best fits of Eq. (3) to the line profiles: $m$ = (a) 0.83 and (b) 0.48. To make a comparison of the intensities at 304 and 77 K convenient, the amplitude of the high-frequency peak at 77 K is taken equal to 100.

ness $A$ and the anisotropy constant $K_u$ characterizing the uniaxial magnetic anisotropy energy $K_u\sin^2\theta$ [7], as

$$\lambda = 4(A/K_u)^{1/2}K(m)m^{1/2}. \quad (2)$$

Thus far, an occurrence of the spin-modulated structure in $BiFeO_3$ has not been confirmed experimentally by the direct microscopic methods other than the neutron diffraction technique. Indirect experimental evidence for the existence of the spiral structure is provided by the fact that $BiFeO_3$ does not exhibit the linear magnetoelectric effect [8], although it is "allowed" by crystal symmetry. The absence of this effect was explained in [8] by the occurrence of the cycloidal structure.

Information on the properties of modulated structures can be extracted from the local-field NMR spectra, because the $L(\theta)$ dependence should modify the NMR line shape, compared to that in the absence of such a dependence. Our study was also motivated by the lack of literature NMR data for $BiFeO_3$.

An attempt at detecting the natural abundance $^{57}$Fe (2.19%) NMR signal in $BiFeO_3$ was unsuccessful. For this reason, a sample enriched with the $^{57}$Fe isotope to 95.43% was prepared using standard ceramic technology. X-ray diffraction analysis suggested that the composition of the sample corresponded to the perovskite-like $BiFeO_3$ phase in which the rhombohedral unit cell parameters $a$ = 3.960(3) Å and $\alpha$ = 89°56(3)′ coincided with the literature data. Zero-field NMR was observed by recording nuclear spin echo amplitude using a pulsed radiospectrometer with frequency scan. The pulses of 8–10 μs duration excited a frequency band of order 0.1 MHz. The time delay between the pulses was chosen to be as small as possible to minimize the effect of spin–spin relaxation time distribution on the echo amplitude.

The first results of our spectral studies at a temperature of 77 K were published in [9, 10]. The theoretical analysis of the NMR line shape was carried out for $BiFeO_3$ in the same works.

This work reports the results of our further NMR studies of $BiFeO_3$ over a wide temperature range from nitrogen to room temperature. The intermediate temperatures were produced by nitrogen blow-through and automatic temperature stabilization to within ±0.15 K.

The $^{57}$Fe spin-echo spectra are shown in Fig. 1 for the two extreme temperatures: 77 and 304 K. For all temperatures, the spectrum is extended over a certain frequency range and consists of two side peaks of different height and a characteristic dip in between. The spectra of this type are typical for the samples with spatially distributed frequencies, e.g., for the NQR and NMR spectra of incommensurate phases in dielectrics [11] and the $CuGeO_3$ system with spin Peierls transition [12], as well as for NMR in domain walls [13].

As shown in our works [9, 10], the expression for the NMR line shape in $BiFeO_3$ has the form (in the δ-function approximation)

$$P(\nu) \sim \{(\nu_\parallel - \nu)^{1/2}(\nu - \nu_\perp)^{1/2} \times [1/m - (\nu - \nu_\perp)/\delta\nu]^{1/2}\}^{-1}, \quad (3)$$

where $\nu$ is the running frequency; $\nu_\parallel$ and $\nu_\perp$ are the $^{57}$Fe NMR frequencies corresponding to $\mathbf{L} \parallel c$ ($\theta = 0$) and $\mathbf{L} \perp c$ ($\theta = \pi/2$), respectively; $\delta\nu = \nu_\parallel - \nu_\perp$ is the frequency difference arising due to the local-field ($H_n$) anisotropy caused by the spin rotation from $\theta = 0$ to $\theta = \pi/2$; and $m$ is the parameter of the elliptic Jacobi function in Eq. (1). The $P(\nu)$ function is defined within the $\nu_\perp < \nu < \nu_\parallel$ interval and is zero for other $\nu$ values.

It is worth noting that Eq. (3) does not allow for the finiteness of local line shape and, strictly speaking, only applies to the steady-state NMR line shapes when the relaxation processes can be ignored. Nevertheless, as a first approximation, we restrict ourselves to this simplest description of the experimental line profile.

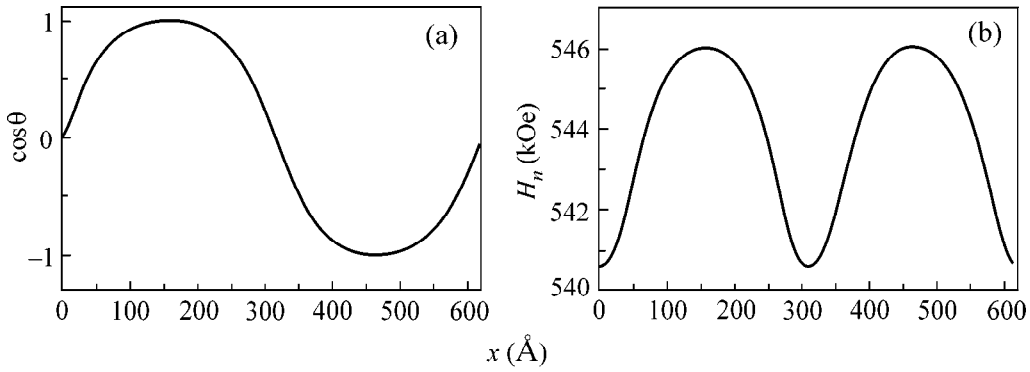


**Fig. 2.** (a) Plot of cos θ vs. *x* coordinate along the propagation direction of the cycloid wave; the soliton character of the spin structure is demonstrated. (b) Plot of local magnetic field $H_n$ at the $^{57}$Fe nuclei vs. the same coordinate, from which the origin of the asymmetry of the NMR peaks becomes clear. The *x* coordinate is measured from the θ = π/ point; the λ = 620 Å period is taken from [5]; *T* = 77 K.

It follows from Eq. (3) that for $m \longrightarrow 0$ the spectrum becomes symmetric, with two equal-intensity side peaks and a minimum half between $\nu_\perp$ and $\nu_\parallel$ (the harmonic cycloidal spin arrangement). At the same time, the distribution becomes more and more anharmonic as $m \longrightarrow 1$. The height ratio of the high-frequency peak at $\nu_\parallel$ to the low-frequency peak at $\nu_\perp$ should increase, while the dip minimum should shift to $\nu_\perp$. One can see that the spectra in Fig. 1 correspond to the hitherto unknown anharmonic spatial distribution of spins. The use of Eq. (3) for line-shape fitting showed that the best agreement with the experiment is achieved with $m \approx 0.83$ and $m \approx 0.48$ for temperatures 77 and 304 K, respectively. These data are evidence that the cycloidal spin distribution becomes more harmonic with a rise in temperature.

The anharmonicity and the soliton-like character of spatial spin modulation are illustrated in Fig. 2a, where dependence (1) is shown for $m = 0.83$ (77 K) and cycloid period of λ = 620 Å taken from the neutron diffraction data [5]. In Fig. 2b, the plot of local field $H_n = (2\pi/\gamma)\nu$ at the $^{57}$Fe nuclei vs. coordinate *x* along the magnetic cycloid period is constructed for 77 K with allowance made for the fact that the local-field anisotropy in a uniaxial crystal is described by formula $H_n(\theta) = (H_n)_\parallel \cos^2\theta + (H_n)_\perp \sin^2\theta$, with the relationship between the θ angle and the *x* coordinate given by Eq. (1) (the gyromagnetic ratio of $^{57}$Fe is $\gamma/2\pi = 0.138$ MHz/kOe). The curve in Fig. 2b clearly demonstrates why the NMR spectrum is asymmetric: the $H_n$ density, being inversely proportional to the $dH_n/dx$ derivative for the nuclei arranged along the *x* coordinate, is higher in the vicinity of the high-frequency peak than near the low-frequency peak. The value of 5.43 kOe ($\delta\nu = 0.75$ MHz) found for the local-field anisotropy at 77 K comprises almost exactly 1% of the total field at the nucleus. This value is comparable with the anisotropy $\delta\nu \approx 0.5$ MHz observed for spin reorientation in the domains [14] and domain walls [13] in rare-earth orthoferrites.

**Table**

| *T*, K ± 0.15 | $\nu_\perp$, MHz ± 0.01 | $\nu_\parallel$, MHz ± 0.01 | δν, MHz ± 0.02 |
|---|---|---|---|
| 77 | 74.60 | 75.35 | 0.75 |
| 130 | 73.75 | 74.50 | 0.75 |
| 160 | 73.18 | 73.90 | 0.72 |
| 180 | 72.54 | 73.30 | 0.76 |
| 210 | 71.68 | 72.47 | 0.79 |
| 240 | 70.40 | 71.20 | 0.80 |
| 260 | 69.35 | 70.15 | 0.80 |
| 296 | 67.70 | 68.47 | 0.77 |
| 304 | 67.08 | 67.88 | 0.80 |

The frequencies $\nu_\perp$ and $\nu_\parallel$ and the anisotropy δν are presented in the table for different temperatures. Within the experimental error, the δν value can be taken to be constant in the temperature range studied. With an increase in temperature, the $\nu_\perp$ and $\nu_\parallel$ frequencies decrease in parallel, in proportion to a decrease in the magnetic moment of the $Fe^{3+}$ ion.

Equation (2) allows one to estimate the uniaxial anisotropy constant $K_u$ using the *m* value derived from the spectra. Assuming $m = 0.48$ (room temperature), $K(0.48) = 1.84$, and $\lambda = 620 \pm 20$ Å [5], and estimating the exchange stiffness as $A \approx (3/2)(k_B T_N/a_{Fe-Fe}) \approx 3.4 \times 10^{-6}$ erg/cm ($T_N$ = 653 K and interatomic distance $a_{Fe-Fe}$ = 4 Å [2]), one obtains from Eq. (2) $K_u \approx 2 \times 10^6$ erg/cm$^3$.

This work was supported by the Russian Foundation for Basic Research, project nos. 98-02-16842 and 98-02-17197.

## REFERENCES


1. Yu. N. Venevtsev, V. V. Gagulin, and V. N. Lyubimov, *Ferroelectric Ferromagnets* (Nauka, Moscow, 1982).
2. J. M. Moreau, C. Michel, R. Gersdon, and W. J. James, J. Phys. Chem. Solids **32**, 1315 (1971).
3. J. D. Bucci, B. K. Roberston, and W. J. James, J. Appl. Crystallogr. **5**, 187 (1972).
4. S. V. Kiselev, R. P. Ozerov, and G. S. Zhdanov, Dokl. Akad. Nauk SSSR **145**, 782 (1962) [Sov. Phys. Dokl. **7**, 712 (1963)].
5. I. Sosnowska, T. Peterlin-Neumaier, and E. Steichele, J. Phys. C: Solid State Phys. **15**, 4835 (1982).
6. I. Sosnovska, M. Loewenhaupt, W. I. F. David, *et al.*, Physica B (Amsterdam) **180/181**, 117 (1992).
7. I. Sosnovska and A. K. Zvezdin, J. Magn. Magn. Mater. **140–144**, 167 (1995).
8. Yu. F. Popov, A. K. Zvezdin, G. P. Vorob'ev, *et al.*, Pis'ma Zh. Éksp. Teor. Fiz. **57**, 65 (1993) [JETP Lett. **57**, 69 (1993)].
9. A. A. Bush, A. A. Frolov, V. S. Pokatilov, *et al.*, in *Proceedings of Moscow International Symposium on Magnetism, Moscow, 1999*, p. 121.
10. A. V. Zalessky, A. A. Frolov, T. A. Khimich, *et al.*, Europhys. Lett. **50**, 547 (2000).
11. I. P. Alexandrova, in *Incommensurate Phases in Dielectrics*, Ed. by R. Blinc and A. P. Levanyuk (North-Holland, Amsterdam, 1986), p. 277.
12. M. Horvatic, C. Berthier, Y. Fagot-Revurat, *et al.*, Physica B (Amsterdam) **246/247**, 22 (1998).
13. A. V. Zalesskiĭ, A. K. Zvezdin, I. S. Zheludev, *et al.*, Phys. Status Solidi B **73**, 317 (1976).
14. A. S. Karnachev, Yu. I. Klechin, N. M. Kovtun, *et al.*, Zh. Éksp. Teor. Fiz. **78**, 1176 (1980) [Sov. Phys. JETP **51**, 592 (1980)].


*Translated by V. Sakun*

*JETP Letters, Vol. 71, No. 11, 2000, pp. 469–472. Translated from Pis'ma v Zhurnal Éksperimental'noĭ i Teoreticheskoĭ Fiziki, Vol. 71, No. 11, 2000, pp. 687–692.*


# Concentration Dependence of the Anomalous Hall Effect in $Fe/SiO_2$ Granular Films below the Percolation Threshold

**B. A. Aronzon*, A. B. Granovskiĭ**, D. Yu. Kovalev*, E. Z. Meĭlikhov*, V. V. Ryl'kov*, and M. V. Sedova*****

** Russian Research Centre Kurchatov Institute, pl. Kurchatova 1, Moscow, 123182 Russia*
*e-mail: rylkov@imp.kiae.ru*
*** Moscow State University, Moscow, 119899 Russia*
**** Institute of Theoretical and Applied Electrodynamics, Moscow, 127412 Russia*
Received April 25, 2000

The anomalous Hall effect is studied on $Fe_x(SiO_2)_{1-x}$ nanocomposite films with $x < 0.7$ in the vicinity of the percolation transition ($x_c \approx 0.6$). It is found that, as the transition is approached from the side of metallic conduction, the Hall angle nonmonotonically varies, passing through a minimum. A qualitative model for describing the concentration dependence of the anomalous Hall effect is proposed. The model is based on that of the conductivity of a two-phase system near the percolation threshold [9, 10]. The anomalous Hall effect is governed by two conduction channels: one of them (a conducting network) is formed by large metal clusters that are separated by narrow dielectric interlayers below the percolation threshold, and the other is represented by the dielectric part of the medium containing Fe grains; in this part of the medium, the anomalous Hall effect occurs through the interference of amplitudes from the tunneling junctions in a set of three grains. It is shown that, at $x < x_c$, the network may give rise to a "shunting" effect, which makes the effective Hall voltage even less than the Hall voltage of the dielectric component. © *2000 MAIK "Nauka/Interperiodica".*

PACS numbers: 73.50.Jt; 72.80.Tm

Ferromagnetic materials are characterized by the Hall field $E_y$ consisting of two components, one of which (the normal component) is caused by the Lorentz force, and the other (the anomalous one) is related to the effect of the spin-orbit interaction on the scattering of spin-polarized electrons and may exceed the normal component by many orders of magnitude [1, 2]. Recently, it was found that the same feature is characteristic of nanocomposites that consist of randomly arranged metallic ferromagnetic inclusions of dimensions 1–10 nm and a dielectric medium filling the space between them [3, 4]. From the studies of the dependence of the Hall resistivity $\rho_h$ in these materials on the metal content $x$ above the percolation threshold [3, 4], it was found that, near the threshold ($x \approx x_c$), the value of $\rho_h$ can be four orders of magnitude greater than in the homogeneous case ($x = 1$). The Hall effect observed in these conditions was called the "giant" Hall effect. We note that the existing percolation models predict an increase in $\rho_h$ by approximately an order of magnitude, although, in principle, by taking into account the strong electron scattering from the intergrain barriers, it is possible to reach an agreement with the experiment [5].

Despite the giant values of $\rho_h$, the studies of the anomalous Hall effect have mainly been performed on nanocomposites with metallic conduction, and the scarce data obtained for dielectric samples ($x \le x_c$) are contradictory. For example, the results obtained by studying a $Ni/SiO_2$ dielectric sample show that $\rho_h$ is saturated near the transition; i.e., it weakly depends on $x \le x_c$ [3]. However, the data obtained for several Co/AlO samples with different types of conductivity (metallic and dielectric ones), but with close values of $x \approx x_c$, testify that $\rho_h$ sharply decreases below the percolation threshold [6]. In our previous experiments, we studied the Hall effect in $Fe/SiO_2$ nanocomposites with a dielectric-type conduction [7]. We managed only to show that the Hall effect was anomalous and studied its dependence on temperature.

Thus, two fundamental issues remain to be clarified: (1) How are the anomalous Hall effect data matched at the transition through the percolation threshold; i.e., does the Hall effect cease being a giant one? (2) What are the main factors that govern the behavior of the anomalous Hall effect near the percolation threshold?

In reality, it is more natural to characterize the Hall effect not by the Hall resistivity $\rho_h$ but by the Hall angle $\beta$, which proves to be a more informative parameter in the case of high-resistance objects (when it is necessary to reduce the current through the sample and switch to the measurements at constant voltage).[1]

[1] For example, in the case of hopping conduction in a doped semiconductor, $\rho_h$ exponentially increases farther into the dielectric region and $\beta$ becomes an exponentially small quantity [8]. Hence, it is not surprising that there still exist no experimental data on the hopping Hall effect in such percolation systems [8].

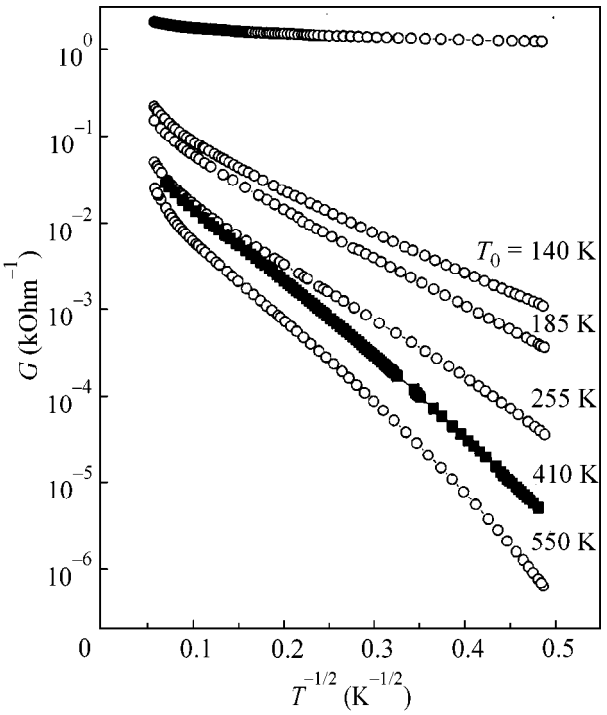


**Fig. 1.** Temperature dependences of the conductivity for samples with the dielectric (with different values of $T_0$) and metallic types of conduction ($x \approx 0.7$). (■) The temperature dependence of the conductivity for a sample obtained on a substrate heated up to $T \approx 170$°C.

Therefore, in this paper we mainly analyze the Hall angle β and its concentration dependence near the percolation transition rather than the Hall resistivity $\rho_h$. The results show that, as the percolation transition is approached from the side of metallic conduction, the Hall angle β sharply decreases and passes through a minimum as the measurements go farther into the dielectric region. The unusual behavior of the Hall effect is explained by the specific features of the conduction of a two-phase system near the percolation threshold [9, 10].

The samples were fabricated in the standard form of a double Hall cross. The width of the conducting channel was $W = 2$ mm and the length was $L = 7$ mm. The thickness of the Fe/$SiO_2$ films varied within the range $d = 0.2$–$0.8$ μm. The samples were prepared in two ways: without heating the substrate in the process of the sample fabrication and by heating the substrate to a temperature of $T \approx 170$°C. The results of the structure analysis of these samples were described in [11]. Here, it should be noted that the films were characterized by a wide distribution of grains in size and by the presence of a fine-grained metal phase that could not be resolved by an electron microscope. These features are typical of a wide class of granular systems, which is confirmed by the recent studies of NiFe/$SiO_2$ [4] and Co/AlO [12] films.

The Hall measurements were performed in magnetic fields up to 10 kOe at temperatures $T = 77$–$300$ K at a constant voltage $V_x = 5$ V. To characterize the samples according to their closeness to the transition, we also studied the temperature dependences of the conductivity $G = I_x/V_x$ ($I_x$ is the current through the sample). Figure 1 presents the dependences $G(T)$ for several dielectric samples with Fe content close to the percolation threshold ($x \le x_c \approx 0.6$); these samples were obtained without the substrate heating. For comparison, we also present the dependences $G(T)$ for a metallic sample with $x \approx 0.7$ and for a dielectric sample that was prepared on a substrate heated to $T \approx 170$°C. For all dielectric samples, the dependences $G(T)$ are virtually linear in the $\log(G)$–$T^{-1/2}$ coordinates in a wide temperature range; hence, the substrate heating does not crucially affect the form of the dependence $G(T)$. This fact is related to the wide distribution of grains in size [13], because such a distribution leads to the 1/2-law for the conductivity: $G(T) = G_0\exp[-(T_0/T)^{1/2}]$, where the parameter $T_0$ is determined by the metal content. The parameter $T_0$ is a more reliable characteristic of the sample's closeness to the percolation transition than the sample composition, because the latter is usually determined with a relatively low accuracy [7]. We note that, in a metallic sample, the conductivity exhibits a power-law decrease with temperature, which is typical of samples that approach the percolation transition from the side of metallic conduction [3].

The anomalous Hall effect was studied in magnetic fields 8–10 kOe in the conditions at which the magnetization $M$ reaches its limiting value and weakly depends on temperature [6]. The Hall resistance $R_h$ was determined from the difference between the values of the transverse resistance $R_{xy} = V_y/I_x$ ($V_y$ is the voltage between the Hall probes) that correspond to the positive ($R_{xy}^+$) and negative ($R_{xy}^-$) directions of the magnetic field: $R_h = (R_{xy}^+ - R_{xy}^-)/2$; the Hall angle was determined by the formula $\beta = E_y/E_x = R_hGL/W$.

The dependence of the Hall angle on the parameter $T_0$ is shown in Fig. 2; the inset shows the curve for the Hall resistivity $\rho_h = R_hd$. One can see that, in the transition region, β steeply decreases with $T_0$ and the dependence $\beta(T_0)$ exhibits a minimum. In the region where β decreases, the Hall resistivity flattens out with a tendency to form a new plateau with increasing $T_0$. The plateaus in the $S_h(T_0)$ dependences are most pronounced at room temperature; the resistivity values corresponding to them differ by approximately a factor of four. We note that the saturation of the dependence $\rho_h(x)$ on the metallic side of the percolation transition was observed for the Ni/$SiO_2$ system and interpreted as the limiting value of the Hall resistivity [3]. However, the data presented in the inset of Fig. 2 testify to a further growth of $\rho_h$ in the dielectric region. We also note

that, for the sample obtained on a heated substrate, the Hall angle is about an order of magnitude less than for similar samples prepared without the substrate heating.

For semiconductors, it is well known that the Hall effect in the hopping regime occurs as a result of the interference of amplitudes from the tunneling transitions in a set of three centers [14]. The results [14] were generalized in [15], where it was shown that, in the presence of the spin-orbit interaction in a system with hopping conduction and magnetization, the anomalous Hall effect is governed by a similar mechanism. Using the approach from [15] and taking into account that, in our case, the grains are distributed in size and the Hall effect is determined by sets of three grains of optimal size [6], we derive the parametric relationship between the Hall $\rho_h$ and the longitudinal $\rho_{xx}$ resistivities (the parameter is temperature): $\rho_h \propto \rho_{xx}^m$; $m \approx 0.6$. This relationship fits the experimental results well.

One would expect that, by taking into account the wide distribution of grains in size and the possibility of their clustering near the percolation threshold, one could also explain the concentration dependence of the Hall effect. In fact, a composite is a two-component medium with one of its components being a weakly conducting phase that consists of the $SiO_2$ dielectric and the isolated Fe grains. The other component is represented by metal clusters forming a conducting network which transforms into an infinite metal cluster when $x > x_c$; on the dielectric side of the transition, this component consists of large metal aggregates (of size about the correlation radius $L$ of a percolation cluster) separated by narrow dielectric interlayers (Fig. 3). The contribution to the Hall effect can be made by both the conducting network and the weakly conducting dielectric phase [6]. Therefore, the anomalous Hall effect that occurs in such a system should be considered in terms of a two-band model [10, 16], which takes into account two conduction channels. In the framework of this model, we obtain the following expression for the Hall resistivity:

$$\rho_h = \frac{\rho_n\sigma_n^2 + \rho_d\sigma_d^2}{(\sigma_n + \sigma_d)^2} \approx \rho_m + \rho_d\frac{\sigma_d^2}{\sigma^2(x)}, \qquad (1)$$

where $\rho_n$ and $\rho_d$ are the Hall resistivities of the network and the dielectric component, respectively; $\sigma_n$ and $\sigma_d$ are their conductivities; $\sigma(x) = (\sigma_n + \sigma_d)$ is the effective conductivity of the medium, which monotonically decreases with decreasing metal content $x$ (i.e., with increasing $T_0$ when $x < x_c$); and $\rho_m$ is the Hall resistivity of the bulk metal.[2] In Eq. (1), we took into account that

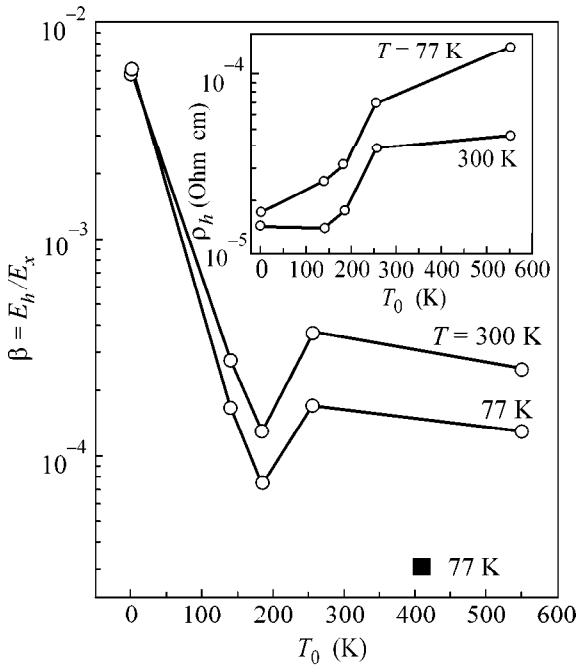


**Fig. 2.** Dependences of the Hall angle tangent and the Hall resistivity (inset) on the parameter $T_0$ at different temperatures. The dependences are obtained in a magnetic field $H$ = 8.4 kOe. The dots on the curves at $T_0 = 0$ correspond to a sample with the iron content $x \approx 0.7$; the dark square (■) shows the tangent of the Hall angle at $T$ = 77 K for a sample prepared on a substrate heated up to 170°C.

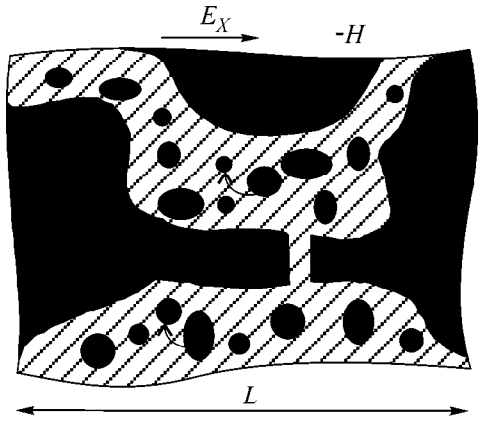


**Fig. 3.** Typical fragment of the medium within the correlation radius $L$. The dielectric component containing the fine-grained metal phase is shown by hatching; the black areas represent the metal clusters. The direction of the electron tunneling is shown by arrows.

$\sigma_d \ll \sigma_n \sim \sigma_m$, where $\sigma_m$ is the conductivity of metal; in addition, we ignored the difference between the Hall fields in the interlayers and in the metal necks; in this case, we have $\rho_n \approx \rho_m$. Using Eq. (1), we obtain

$$\beta = H\left(\frac{\mu_m}{\sigma_m}\right)\left[\sigma(x) + \frac{\mu_d\sigma_d\sigma_m}{\mu_m\sigma(x)}\right], \qquad (2)$$

[2] In [10], the Dykhne method [9] is used to obtain the exact results for the Hall effect in the case of a 2D two-component system; these results lead to Eq. (1) when the conditions $\sigma_m/\sigma_d \gg 1$ and $\sigma_m^2/\sigma_d^2 \gg \rho_d/\rho_m \gg 1$ are fulfilled.

where $\mu_m$ and $\mu_d$ are the Hall mobilities of the metallic and dielectric components, respectively.

Eq. (2) predicts a minimum in the dependence of $\beta$ on $\sigma(x)$: when $\sigma(x)$ decreases and $\sigma(x) \longrightarrow \sigma_d$, the quantity $\beta$ tends to a constant value $\beta = H\mu_d$ determined by the Hall mobility of the dielectric component. According to [9, 10], in the special case $\mu_m = \mu_d$, the minimum should be observed at $x = x_c$, with the conductivity taking the value $\sigma_{\min} = \sigma_c = (\sigma_m\sigma_d)^{1/2}$. In the case under study, the mobility of the dielectric component is obviously less than $\mu_m$ (see Fig. 2), and from Eq. (2) it follows that $\sigma_{\min} = (\mu_d\sigma_m\sigma_d/\mu_m)^{1/2}$; i.e., $\sigma_{\min}$ is less than $\sigma_c$. Hence, no wonder that the minimum occurs below the percolation threshold where $\sigma$ exhibits an activation-type temperature dependence.

It is evident that the minimum in the curve $\beta(T_0)$ is caused by the effects of Hall field shunting by the metal clusters, these effects being most pronounced in the vicinity of the percolation threshold at $\sigma \sim \sigma_{mi}$. Basically, this is a consequence of the specific features of the Hall effect in the two-channel conduction regime. In our case, the contribution made by the conducting network to the Hall voltage decreases with a decrease in its conductivity (see Eq. (2)). When this contribution becomes less than the contribution of the dielectric component while the conductivity of the network is still high as compared to $\sigma_d$, the Hall voltage of the dielectric component is shunted.

In these conditions, one should expect a saturation of the Hall resistivity, which is observed in the experiments described above (Fig. 2), as well as in other experiments [3]. However, as one moves farther into the dielectric region, the distance between the metal clusters increases and the clusters themselves are divided into smaller ones; as a result, the effects of Hall field shunting are suppressed. Therefore, with increasing $T_0$, the $\rho_h(T_0)$ dependence exhibits a rise with a tendency to form a new plateau (Fig. 2), which, according to Eq. (1), is determined by the Hall resistivity of the weakly conducting dielectric component.

In terms of the model under consideration, it is also possible to explain the role of the substrate heating in the process of the sample preparation. The heating (annealing) of nanocomposite samples is accompanied by the growth of the metal clusters through a decrease in the content of the fine-grained metal phase. In this case, the contribution of the dielectric component to the Hall voltage should be suppressed. Hence, it is not surprising that the Hall angle obtained for the sample prepared on a heated substrate is noticeably less than the Hall angles obtained for the samples prepared without heating (Fig. 2).

In closing, we note that, in the absence of a wide distribution of particles in size, one should expect a smaller contribution of the dielectric component to the Hall voltage and, hence, a sharper drop in the Hall angle. In this case, the saturation observed in the dependence $\rho_h(x)$ at $x \le x_c$ may give way to a decrease, which, presumably, was the case in the experiments described in [5].

We are grateful to A.K. Sarychev and A.A. Snarskiĭ for discussions and valuable remarks. This work was supported by the Russian Foundation for Basic Research (project nos. 99-02-16955 and 00-02-17191) and the PICS Russian–French Foundation (project no. 98-02-22037).

## REFERENCES

1. R. M. White and T. H. Geballe, *Long Range Order in Solids* (Academic, New York, 1979).
2. A. V. Vedyaev, A. B. Granovskiĭ, and O. A. Kotel'nikova, *Kinetic Phenomena in Disordered Ferromagnetic Alloys* (Mosk. Gos. Univ., Moscow, 1992).
3. A. B. Pakhomov, X. Yan, and Y. Xu, J. Appl. Phys. **79**, 6140 (1996); A. B. Pakhomov and X. Yan, Solid State Commun. **99**, 139 (1996).
4. A. B. Pakhomov, X. Yan, N. Wang, *et al.*, Physica A (Amsterdam) **241**, 344 (1997).
5. F. Brouers, A. Granovsky, A. Sarychev, *et al.*, Physica A (Amsterdam) **241**, 284 (1997).
6. H. Sato, Y. Kobayashi, K. Hashimoto, *et al.*, J. Magn. Soc. Jpn. **23**, 73 (1999).
7. B. A. Aronzon, D. Yu. Kovalev, A. N. Lagar'kov, *et al.*, Pis'ma Zh. Éksp. Teor. Fiz. **70**, 87 (1999) [JETP Lett. **70**, 90 (1999)].
8. Yu. M. Gal'perin, E. P. German, and V. G. Karpov, Zh. Éksp. Teor. Fiz. **99**, 343 (1991) [Sov. Phys. JETP **72**, 193 (1991)].
9. A. M. Dykhne, Zh. Éksp. Teor. Fiz. **59**, 641 (1970) [Sov. Phys. JETP **32**, 348 (1970)].
10. B. I. Shklovskiĭ, Zh. Éksp. Teor. Fiz. **72**, 288 (1977) [Sov. Phys. JETP **45**, 152 (1977)].
11. B. A. Aronzon, A. E. Varfolomeev, D. Yu. Kovalev, *et al.*, Fiz. Tverd. Tela (St. Petersburg) **41**, 944 (1999) [Phys. Solid State **41**, 857 (1999)].
12. S. Mitani, S. Takahashi, K. Takanashi, *et al.*, Phys. Rev. Lett. **81**, 2799 (1998).
13. E. Z. Meĭlikhov, Zh. Éksp. Teor. Fiz. **115**, 1484 (1999) [JETP **88**, 819 (1999)].
14. T. Holstein, Phys. Rev. **124**, 1329 (1961).
15. A. V. Vedyaev and A. B. Granovskiĭ, Fiz. Tverd. Tela (Leningrad) **28**, 2310 (1986) [Sov. Phys. Solid State **28**, 1293 (1986)].
16. A. A. Snarskiĭ, Zh. Éksp. Teor. Fiz. **91**, 1405 (1986) [Sov. Phys. JETP **64**, 828 (1986)].

*Translated by E. Golyamina*

JETP Letters, Vol. 71, No. 11, 2000, pp. 473–476. From Pis'ma v Zhurnal Éksperimental'noĭ i Teoreticheskoĭ Fiziki, Vol. 71, No. 11, 2000, pp. 693–697.


# Observation of the Parallel-Magnetic-Field-Induced Superconductor–Insulator Transition in Thin Amorphous InO Films[1]

**V. F. Gantmakher, M. V. Golubkov, V. T. Dolgopolov, A. A. Shashkin, and G. E. Tsydynzhapov**

*Institute of Solid-State Physics, Russian Academy of Sciences, Chernogolovka, Moscow region, 142432 Russia*

*e-mail: gantm@issp.ac.ru*

Received April 25, 2000

We study the response of a thin superconducting amorphous InO film with variable oxygen content to a parallel magnetic field. A field-induced superconductor–insulator transition (SIT) is observed that is very similar to the one in normal magnetic fields. As the boson-vortex duality, which is the keystone of the theory of the field-induced SIT, is obviously absent in the parallel configuration, we have to draw a conclusion about the theory's insufficiency. © *2000 MAIK "Nauka/Interperiodica".*

PACS numbers: 74.80.Bj; 74.76.Db

A good deal of work was performed on the investigation of the magnetic-field-induced superconductor–insulator transition (SIT) on superconducting amorphous films of InO [1–3], MoGe [4], and MoSi [5] with thickness comparable to the superconducting coherence length. It was found that with increasing field $B$ the resistance $R$ of all studied films rises abruptly at a magnetic field $B_c$ and then passes through a maximum followed by a drop in high magnetic fields [2, 3]. The film state just above $B_c$ was identified as insulating, although at the lowest temperatures, about 30 mK, the maximum resistance does not exceed 100 kΩ and the temperature dependences of $1/R$ correspond to the activation energies which do not exceed by far the lowest temperatures. Near $B_c$, at sufficiently low temperatures, the resistance $R(T, B)$ was found to be a function of the single scaling variable $u = (B - B_c)/T^y$ with exponent $y \approx 0.8$. The above experimental findings are regarded as confirming the theory of the quantum SIT [6] in two-dimensional (2D) superconducting films subjected to a normal magnetic field. This theory exploits the concept of the hypothetical system of charged bosons in a random potential and is based on the boson-vortex symmetry of the model Hamiltonian. In the vicinity of the SIT point ($T = 0$, $B = B_c$), the film resistance $R(T, B)$ is expected to be a universal function of the single scaling variable, which is defined as the ratio of the correlation length $\xi \propto (B - B_c)^{-\nu}$ and the dephasing length $L_\phi \propto T^{-1/z}$, where $\nu$ and $z$ are the critical indices. The form of the scaling variable implies that the value $1/z\nu$ has to be identified with exponent $y$. The concept of the localization of electron pairs, or bosons [6], has been supported recently by the work of [7]. There, it is shown that for a 2D superconducting film with strong disorder, the region of fluctuation superconductivity, where the electron pairs occur, should extend down to zero temperature. In this region, the unpaired electrons are supposed to be localized, whereas the bosons can be either localized or delocalized, depending on the value of the magnetic field.

Other experimental results were interpreted within the model of electron pair localization: (i) A crossing of Hall isotherms $R_{xy}(B)$ was observed at a field $B_{c0} > B_c$ and attributed to a transition between the Bose insulator and a Fermi insulator that consists of localized single electrons; i.e., pairing was presumed to be destroyed at $B_{c0}$ [1]. (ii) The resistance drop in high fields was explained in terms of the electron pair breaking which occurs gradually with increasing $B$ owing to the different binding energies of bosons in a random potential [2, 3].

However, a very similar SIT has been observed recently on amorphous MoSi films with the thickness $d = 1700$ Å, which is an order of magnitude larger compared to the superconducting coherence length $\xi_{sc}$ [8]. This fact causes one to think that either the theory is inadequate or its restrictions are too severe.

Here, we investigate the influence of a parallel magnetic field on the superconducting properties of a thin amorphous InO film with variable oxygen content. For all film states we find a complete similarity in the behavior of the resistance $R(T, B)$ for both parallel and perpendicular magnetic fields.

The sample is an amorphous InO film with thickness 200 Å that was grown by electron-gun evaporation of a high-purity $In_2O_3$ target onto a glass substrate [9]. Oxygen deficiency compared to fully stoichiometric insulating compound $In_2O_3$ causes the film conductiv-

[1] This article was submitted by the authors in English.

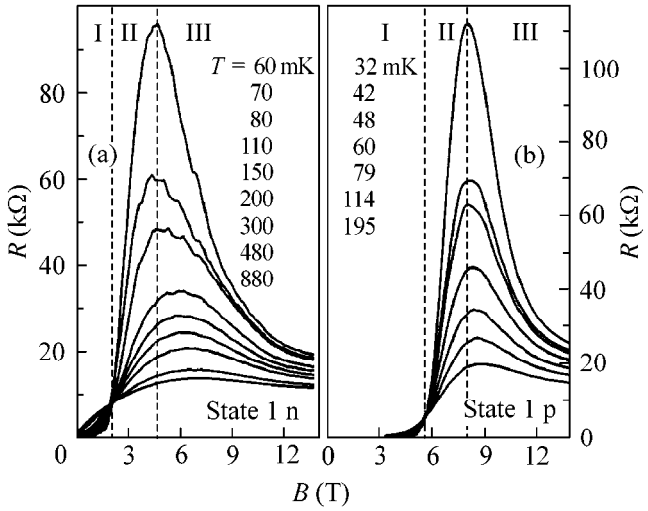


**Fig. 1.** Isotherms $R(B)$ for (a) normal and (b) parallel magnetic field. The dashed lines separate regions I, II, and III and correspond to the critical field $B_c$ and the resistance maximum at the lowest temperatures.

ity. By changing the oxygen content, one can cover the range from a superconducting material ($\xi_{sc} \approx 500$ Å) to an insulator with activated conductance [10]. The procedures to change the film state reversibly are described in detail in [2]. To reinforce the superconducting properties of the film, we used heating in vacuum up to a temperature from the interval 70–110°C until the sample resistance became saturated. To shift the film state in the opposite direction, we made an exposure to air at room temperature. As the film remains amorphous during these manipulations, it is natural to assume that the treatment used results mainly in a change of the carrier density $n$ and that the value $n$ is inversely proportional to the room temperature resistance $R_r$ of the sample. Seven superconducting states of the film were studied.

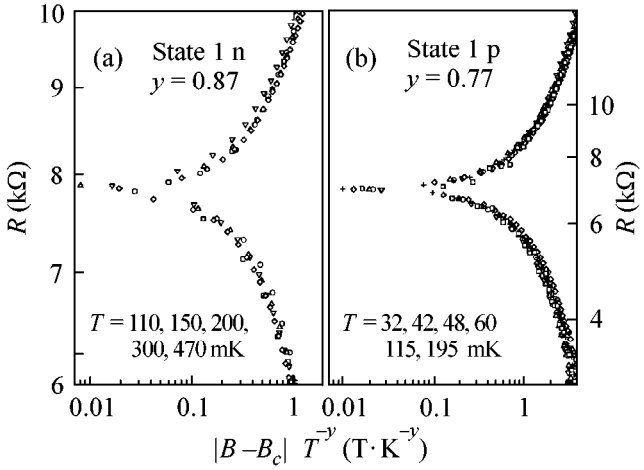


**Fig. 2.** Scaling plot for the (a) normal and (b) parallel magnetic field.

The film was mounted into the top loading system of a dilution refrigerator; it was set either parallel or normal to the magnetic field within 1° accuracy. A four-terminal lock-in technique at a frequency of 10 Hz was used to measure the resistance of the sample. The ac current through the sample was equal to 1 nA.

The experimental dependences $R(B)$ for two close states of the film in the normal and parallel field orientations are presented in Fig. 1. As seen from the figure, for both field orientations the isotherms cross at the critical field $B_c$, which separates the superconducting region I and the insulating region II. The resistance drop with $B$ in region III down to values of about $h/e^2$ indicates that at high magnetic fields the film state is metallic. The critical field $B_c$ is found to vary with field direction by about a factor of two. Nevertheless, near $B_c$, the experimental data collapse onto a single curve equally well for both perpendicular and parallel magnetic fields, with close values of exponent $y$, see Fig. 2.

Figure 3 displays the behavior of the relative resistance maximum $R_{max}/R_{14T}$ at the lowest temperature and of the critical field $B_c$ with changing film state. As seen from the figure, the resistance ratio decreases and approaches unity as one goes deeper into the superconducting phase. The value $B_c$ for both field directions increases when departing from the zero-field SIT, being higher in the parallel configuration.

The mean free path of the normal electrons in our film is small compared to the film thickness [3], and, hence, the metal–insulator transition expected in region III should be three-dimensional. In this case, the conductance $1/R$ in the vicinity of metal–insulator transi-

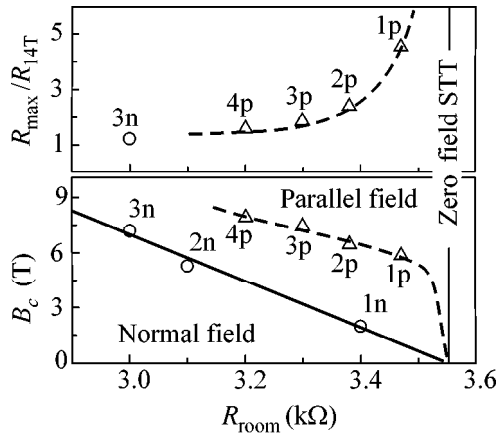


**Fig. 3.** Change of the relative resistance maximum at $T \approx 30$ mK and of the critical magnetic field with changing film state, as determined by the room temperature resistance of the film. The dashed lines are guides to the eye.

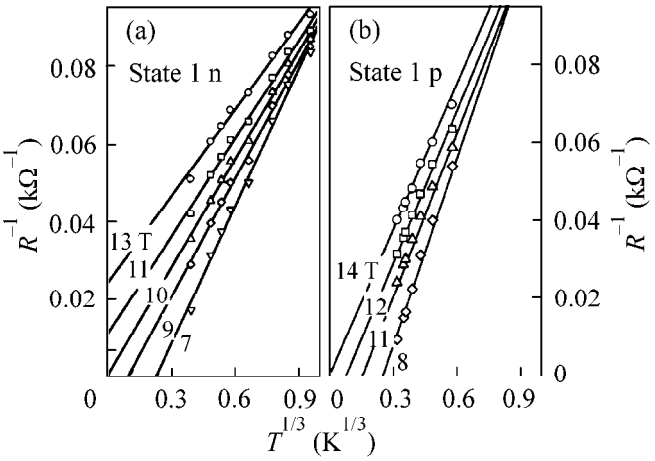


**Fig. 4.** The temperature dependence of $1/R$ near the three-dimensional metal–insulator transition in the (a) normal and (b) parallel magnetic field.

tion is expected to change linearly with $T^{1/3}$ and extrapolation of the linear dependence to $T = 0$ should reveal whether the phase is metallic or insulating, as judged by the offset sign [11, 12]. Such a data analysis is shown in Fig. 4. For both field configurations, the experimental data behave similarly: the offset of the linear dependence increases with $B$, passing through zero at the transition point.

The crucial point of the theory of the magnetic-field-driven SIT [6] is the boson-vortex duality for vortices induced by an external magnetic field penetrating the film, which is not the case for a parallel magnetic field. The experimentally observed complete similarity of the SIT properties in the perpendicular and parallel magnetic fields forces one to conclude that the theory is not directly applicable to actual superconducting systems with disorder.

Nonetheless, assuming that the parallel magnetic field is capable of localizing the fluctuation-induced Cooper pairs in the paraconductivity region, one can translate all experimental findings into the language of localized bosons. We emphasize that the speculations below are very attractive but do not have a sound experimental basis so far.

One can reckon that the resistance rise with $B$ in region II is caused by decreasing boson localization length. Assuming additionally that the magnetic field not only localizes, but also breaks, electron pairs, it is easy to interpret the resistance drop in region III: breaking the correlations in localized electron pairs results in an increase in the electron hopping probability [2] and eventually electron delocalization at high fields [3]. For sufficiently deep film states in the superconducting phase; i.e., sufficiently high $B_c$, at $B > B_c$, the localized bosons coexist with delocalized normal electrons, so that the state never becomes insulating. In other words, as one advances into the superconducting phase, a fraction of the localized bosons reduces. As a result, the relative amplitude of the resistance maximum $R_{max}/R_{14T}$ tends to unity (Fig. 3), and the SIT should transform into an ordinary superconductor to normal metal transition.

In summary, we have investigated the response of a thin superconducting amorphous InO film to a parallel magnetic field. At a critical field $B_c$, a SIT has been observed that is very similar to the one in normal magnetic fields. That the boson-vortex duality is absent in the parallel configuration points to the insufficiency of the theory of the field-induced SIT [6]. We find that the behaviors of the film resistance at fields above the transition are also similar for parallel and normal magnetic fields.

This work was supported by the Russian Foundation for Basic Research, project no. 99-02-16117; the Russian Foundation for Basic Research-PICS, project no. 98-02-22037; and the program "Statistical Physics" of the Russian Ministry of Sciences.

## REFERENCES

1. A. F. Hebard and M. A. Paalanen, Phys. Rev. Lett. **65**, 927 (1990); M. A. Paalanen, A. F. Hebard, and R. R. Ruel, Phys. Rev. Lett. **69**, 1604 (1992).
2. V. F. Gantmakher, M. V. Golubkov, J. G. S. Lok, and A. K. Geim, Zh. Éksp. Teor. Fiz. **109**, 1765 (1996) [JETP **82**, 951 (1996)].
3. V. F. Gantmakher, M. V. Golubkov, V. T. Dolgopolov, *et al.*, Pis'ma Zh. Éksp. Teor. Fiz. **68**, 345 (1998) [JETP Lett. **68**, 363 (1998)]; Pis'ma Zh. Éksp. Teor. Fiz. **71** (2000) (in press) [JETP Lett. **71**, 160 (2000)].

4. A. Yazdani and A. Kapitulnik, Phys. Rev. Lett. **74**, 3037 (1995).
5. S. Okuma, T. Terashima, and N. Kokubo, Solid State Commun. **106**, 529 (1998).
6. M. P. A. Fisher, G. Grinshtein, and S. M. Girvin, Phys. Rev. Lett. **64**, 587 (1990); M. P. A. Fisher, Phys. Rev. Lett. **65**, 923 (1990); S. L. Sondhi, S. M. Girvin, J. P. Carini, and D. Shahar, Rev. Mod. Phys. **69**, 315 (1997).
7. A. I. Larkin, Ann. Phys. (Leipzig) **8**, 785 (1999).
8. A. V. Samoilov, N.-G. Yeh, and C. C. Tsuei, Phys. Rev. B **57**, 1206 (1998).
9. The films were kindly presented by A. Frydman and Z. Ovadyahu from Jerusalem University.
10. D. Shahar and Z. Ovadyahu, Phys. Rev. B **46**, 10917 (1992).
11. Y. Imry and Z. Ovadyahu, Phys. Rev. Lett. **49**, 841 (1982).
12. V. T. Dolgopolov, Pis'ma Zh. Éksp. Teor. Fiz. **68**, 807 (1998) [JETP Lett. **68**, 848 (1998)].

JETP Letters, Vol. 71, No. 11, 2000, pp. 477–480. Translated from Pis'ma v Zhurnal Éksperimental'noĭ i Teoreticheskoĭ Fiziki, Vol. 71, No. 11, 2000, pp. 698–704.


# Phonon–Plasmon Interaction in Tunneling GaAs/AlAs Superlattices

**V. A. Volodin*, M. D. Efremov*, V. V. Preobrazhenskiĭ*, B. R. Semyagin*, V. V. Bolotov**, V. A. Sachkov**, E. A. Galaktionov***, and A. V. Kretinin*****

** Institute of Semiconductor Physics, Siberian Division, Russian Academy of Sciences, pr. akademika Lavrent'eva 13, Novosibirsk, 630090 Russia*

*e-mail: volodin@isp.nsc.ru*

*** Institute of Sensor Microelectronics, Siberian Division, Russian Academy of Sciences, Omsk, 644077 Russia*

**** Novosibirsk State University, ul. Pirogova 2, Novosibirsk, 630090 Russia*

Received May 11, 2000

The phonon–plasmon interaction in tunneling $GaAs_n/AlAs_m$ superlattices ($m = 5$ and $6 \geq n \geq 0.6$ monolayers) was studied by Raman scattering spectroscopy. The interaction of optical phonons localized in GaAs and AlAs layers with quasi-three-dimensional plasmons strengthens as the thickness of GaAs quantum wells decreases and the electronic states in the superlattices become delocalized due to tunneling. It is assumed that the plasmons also interact with the *TO*-like phonon modes localized in quantum islands or in thin ruffled layers. © *2000 MAIK "Nauka/Interperiodica"*.

PACS numbers: 63.20.Ls; 73.20.Dx

The current status of electronics is characterized by a widespread use of submicron technologies and rapid progress in manufacturing nanoelectronic devices. With a decrease in characteristic sizes of semiconductor elements, the role of charge-carrier tunneling increases, which stimulates scientific interest in studying the tunneling phenomena. Tunneling is accompanied by electron delocalization and, hence, alters the properties of an electron subsystem. The modification of the frequency spectrum of the collective electron-gas oscillations is one of the consequences of tunneling. One can expect that the frequency of plasmons with wavevectors directed along the electron-quantization axis increases, giving rise to the changes in the spectrum of phonon–plasmon states. Many works have been devoted to the phonon–plasmon interaction in bulk [1] and in a system of isolated quantum wells [2–7] (see review in [8, 9]). Except for several theoretical works [10, 11] and experimental data on the three-dimensional character of phonon–plasmon states in GaAs/AlAs superlattices with a narrow AlAs barrier [12, 13], these questions were not considered for tunneling superlattices. Among the experimental works, one can cite papers [14, 15], where the phonon–plasmon interaction was analyzed for doped solid solutions $Al_xGaAs_{1-x}$ having a more complicated phonon spectrum than bulky semiconductors do. This work is devoted to studying the phonon–plasmon interaction in tunneling superlattices with narrow GaAs layers.

The experimental $GaAs_n/AlAs_m$ structures were prepared by molecular beam epitaxy on a GaAs substrate with (001) orientation. The AlAs barrier width was equal to 13.6 Å in each sample, while the thickness of the GaAs layers was varied and taken to be 17, 10.2, 6.8, 3.4, and 1.7 Å for the samples numbered *1–5*, respectively. The samples were grown at a substrate temperature of 550°C under the conditions of $(2 \times 4)$ reconstruction for both GaAs and AlAs surfaces [16] and monitoring by high-energy electron diffraction. Two sets of samples were prepared: undoped and doped with silicon to a concentration of $2 \times 10^{18}$ cm$^{-3}$. The undoped and doped superlattices were coated with protective GaAs layers of thicknesses 40 and 250 Å, respectively. The phonon spectrum and the spectrum of mixed phonon–plasmon superlattice modes were studied by Raman scattering spectroscopy. The Raman spectra were recorded at room temperature in quasi-backward scattering geometry $Z[XY]\bar{Z}$ on an automated instrument with a DFS-52 monochromator using the 514.5 nm (2.41 eV) Ar laser line.

The Raman spectra of superlattices in the frequency range of GaAs optical vibrations are shown in Fig. 1. A peak at 291 cm$^{-1}$ observed in the spectra of all superlattices corresponds to the Raman scattering from the longitudinal optical (*LO*) phonons of GaAs bulk in the substrate and the protecting layer. The study of phonon–plasmon interaction in superlattices is hampered by the fact that the number of phonon modes increases with increasing unit-cell size, while the phonon frequencies decrease with a decrease in the layer thickness because of the localization of optical phonons in the GaAs and AlAs layers. The frequencies of localized phonons can be determined from the

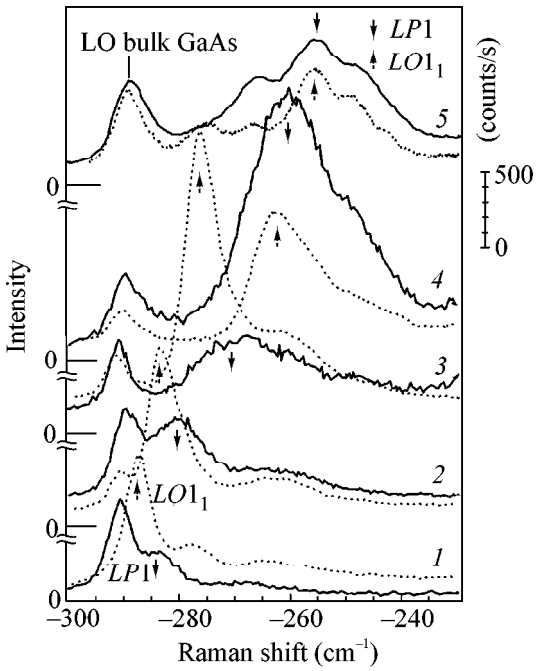


**Fig. 1.** Raman scattering spectra of $GaAs_n/AlAs_m$ superlattices in the range of GaAs-like phonon frequencies; $m = 5$ monolayers; and $n = 6$, 3.6, 2.4, 1.2, and 0.6 monolayers for samples *1*–*5*, respectively (the solid lines are for the doped samples, and the dotted lines are for the undoped samples).

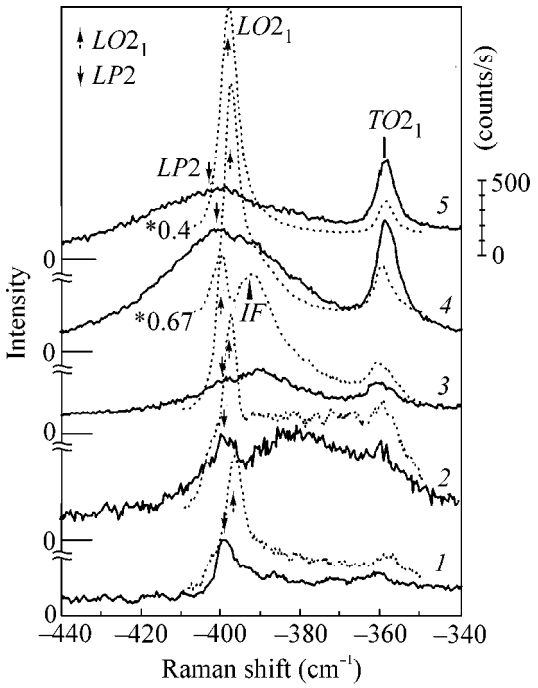


**Fig. 2.** Raman scattering spectra of $GaAs_n/AlAs_m$ superlattices in the range of AlAs-like phonon frequencies (the solid lines are for the doped samples, and the dotted lines are for the undoped samples).

Raman spectra of the undoped lattices, shown in Fig. 1. The appearance of additional peaks in sample *5* (Fig. 1, spectrum *5*) was discussed in [17]. They are due to the lateral localization of optical phonons in the GaAs quantum islands formed in the course of coating the $(2 \times 4)$-reconstructed AlAs surface with a GaAs submonolayer. The spectra of doped superlattices show peaks due to the scattering from the mixed phonon–plasmon modes. In what follows, the first-order Raman lines corresponding to the localized longitudinal modes in the GaAs and AlAs layers are denoted by $LO1_1$ and $LO2_1$, respectively, while the corresponding mixed phonon–plasmon modes in the doped superlattices are denoted by $LP1$ and $LP2$. For instance, in sample *1* with weak tunneling, the $LP1$ line is slightly shifted to lower energies from the $LO1_1$ line (Fig. 1, spectrum *1*), while the $LP2$ line shifts to higher energies relative to the $LO2_1$ line (Fig. 2, spectrum *1*). For the interacting planes of a two-dimensional electron gas, the plasma frequency in the absence of tunneling and the presence of intrasubband transitions is expressed as [3, 4]

$$\omega_p = \left[\frac{2\pi n_S e^2}{\epsilon m^*} k_l \frac{\sinh k_l a}{\cosh k_l a - \cos k_t a}\right]^{1/2},$$

where $n_S$ is the surface density of the electron gas, $a$ is the superlattice parameter, and $k_l$ and $k_t$ are the longitudinal and transverse components of the plasmon wavevector. In the geometry of our experiment, $k_l$ and $k_t$ were equal to $8.65 \times 10^4$ and $1.0 \times 10^6$ cm$^{-1}$, respectively. The value of 28 cm$^{-1}$ estimated for the plasma frequency is too small for the observed line shifts to be interpreted. One can assume that these shifts are due to the interaction between phonons and plasma oscillations with the participation of the intersubband transitions. Indeed, the corresponding theoretical treatment [5] provides the low- and high-energy shifts for the *LP* modes in GaAs and AlAs, respectively. On further thinning of the GaAs layers, the $LP1$ line broadens and shifts from $LO1$ to lower frequencies (Fig. 1, spectra *1*–*3*). The $LP2$ line shift is less pronounced. Such a behavior corresponds to the delocalization of electron wave functions, when the plasma frequency can appreciably increase even if only the intrasubband transitions occur. In this case, the plasmons efficiently interact with the phonons localized in the gallium arsenide layer. For the superlattices with thin GaAs layers, the spectra of the doped and undoped samples virtually coincide in the range of GaAs-type vibrations (Fig. 1, spectra *4*, *5*). The reverse is observed for the *LO* phonons localized in the AlAs layers. The $LP2$ line shifts to higher energies and simultaneously broadens (Fig. 2, spectra *4*, *5*). This is explained by the further increase in the frequency of plasma oscillations, because the interaction between the plasmons and the phonons localized in the AlAs layers strengthens as the tunneling becomes more efficient.

It should be noted that the spectra of undoped samples *4* and *5* show a rather intense scattering peak due to the localized transverse optical ($TO2_1$) phonons (Fig. 2), although the backward Raman scattering from the (001) surface is forbidden for the transverse modes by symmetry selection rules [4]. The appearance of the "forbidden" *TO* lines may be caused by the fractional filling of the GaAs monolayers (the thickness of the GaAs layer in samples *4* and *5* is equal to 0.6 and 1.2 monolayers, respectively). The superlattices grown on a (2 × 4)-reconstructed surface possess a lateral structure, reflecting the symmetry of surface reconstruction, as is manifested in their Raman spectra [17]. This may violate the Raman selection rules. Moreover, the dipole moment projection on the wavevector direction may be nonzero for the *TO*-like modes in a thin ruffled layer, resulting in the inducing interaction between the *TO*-like modes and the plasma oscillations. As is known, the dipole moment projection on the wavevector direction is zero for the transverse modes in superconductor bulk, and, hence, they do not interact with the plasma oscillations. Indeed, the intensities of transverse modes of samples *4* and *5* are higher for the doped superlattices than for the undoped ones. For example, the Raman intensity for the mixed *TO–LO* modes localized in the GaAs quantum islands increased almost twofold (Fig. 1, spectra *4* and *5*). A certain broadening of the Raman lines is also observed for both transverse modes in AlAs and mixed modes in the GaAs quantum islands. Therefore, one can speak about the interaction between *TO*-like modes and plasmons in the ultrathin ruffled layers.

Apart from the localized modes, the interface (*IF*) modes of two types arise in the superlattices. The first one has the *E* symmetry (*LO* type) and the second has the $B_2$ symmetry (*TO* type) [18]. As the thickness of the GaAs layers decreases, the frequency of the first mode approaches the frequency of the $LO2_1$ mode, while the frequency of the second mode approaches the $TO2_1$ frequency. The $LO2_1$ mode is most pronounced in the spectrum of undoped superlattice *3* (GaAs thickness 6.8 Å). In the superlattices with even thinner GaAs layers (samples *4* and *5*), the frequency of this mode approaches the *LO*1 frequency, so that both are almost unresolved in the spectrum. It is known that the *IF* modes are clearly seen in the resonance Raman spectra [9]. It may well be that the scattering conditions in the cited lattices are close to the resonance Raman conditions. The use of the Kronig–Penney model for calculating the transition energies between the localized states yielded the values of 2.22, 2.42, and 2.55 eV for samples *3–5*, respectively. The Raman frequencies and widths for the *LO*, *TO*, and mixed modes were determined by approximating the experimental spectra with a set of Lorentzians. The results are presented in Fig. 3.

To theoretically calculate the Raman spectra, allowance should be made for the phonon localization in the layers, Coulomb interaction between electrons in the neighboring quantum wells, electron tunneling, and the multicomponent character of the phonon subsystem containing additional localized phonon modes in the optical region of the spectrum. Such a calculation is a challenge, because detailed theoretical analysis of the phonon–plasmon interaction in tunnel-coupled systems is lacking in the literature and because the GaAs/AlAs superlattices can transform to the electronic structure of the type II superlattice upon a decrease in the layer thickness. However, one can assume that the electron and phonon subsystems of AlAs become three-dimensional in the systems with GaAs content less than one monolayer and estimate the plasma frequency. In the three-dimensional case, the frequencies of the mixed $LO_-$ and $LO_+$ modes for $q \approx 0$ are determined as [8]

$$\omega_\pm^2 = \frac{1}{2}\{(\omega_P^2 + \omega_{LO}^2) \pm [(\omega_P^2 - \omega_{LO}^2)^2 + 4\omega_P^2(\omega_{LO}^2 - \omega_{TO}^2)]^{1/2}\},$$

$\omega_P = (4\pi ne^2/\epsilon_\infty m^*)^{1/2}$, where $\omega_P$ is the plasma frequency, $m^*$ is the effective mass, and $\epsilon_\infty$ is the rf permittivity. In the superlattices with ultrathin GaAs layers (samples *4* and *5*), the plasma oscillations interact with the AlAs-like phonons. For the three-dimensional electron concentration of $2 \times 10^{18}$ cm$^{-3}$, the $LO_+$ frequency in GaAs should be equal to 492 cm$^{-1}$. Because of the differences in the electron effective masses (0.068 and 0.5) and the rf permittivities (11.9 and 8.5) of GaAs and

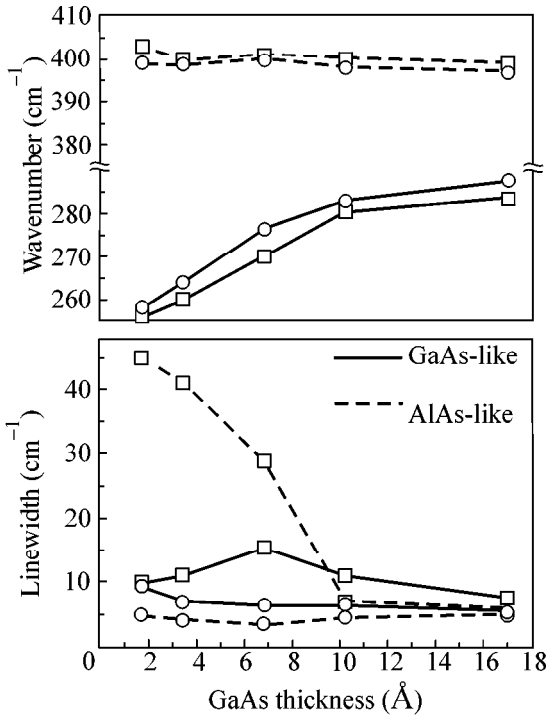


**Fig. 3.** Frequencies and widths of the (○) localized phonon modes and (□) mixed phonon–plasmon modes vs. the GaAs layer thickness.

AlAs, respectively, the plasma frequency in the latter case should be 205 $cm^{-1}$ for the $LO_+$ frequency to be 410 $cm^{-1}$. The experimental frequency for sample *5* with the GaAs layer of submonolayer thickness was found to be 403 $cm^{-1}$. The disagreement is likely caused by an increase in the electron effective mass in the superlattice growth direction. A more precise estimate was carried out with the electron gas susceptibility given by the Lindhard–Mermin expression valid for an arbitrary wavevector and with taking into account that the electron mass in the superlattice growth direction is the largest. The best fit of the calculation to the experiment was achieved when the electron effective mass in the growth direction comprised 1.6 of the bulk mass in AlAs.

The validity of the assumption about the three-dimensional character of the plasmon and phonon spectra can be checked by comparison with the Raman scattering data for doped solid solutions $Al_xCa_{1-x}As$ [14, 15]. The frequency-dependent dielectric constant for these systems is

$$\epsilon(\omega) = \epsilon_\infty\left[1 - \frac{\omega_P^2}{\omega^2} + (1-x)\frac{\omega_{l,\,\mathrm{CaAs}}^2 - \omega_{T,\,\mathrm{GaAs}}^2}{\omega_{T,\,\mathrm{GaAs}}^2 - \omega^2} + x\frac{\omega_{L,\,\mathrm{AlAs}}^2 - \omega_{T,\,\mathrm{AlAs}}^2}{\omega_{T,\,\mathrm{AlAs}}^2 - \omega^2}\right],$$

where $x$ and $(1-x)$ are, respectively, the partial contributions of the AlAs- and GaAs-like phonons (for the superlattices; $x = d_{\mathrm{AlAs}}/d$, where $d$ is the superlattice parameter); and $\omega_P$, $\omega_L$, and $\omega_T$ are the frequencies of plasma oscillations, longitudinal phonons, and transverse phonons, respectively. The value of 403 $cm^{-1}$ observed in [14] for the frequency of $LO_+$ mode in the $Al_{0.86}Ga_{0.14}As$ solid solution (electron concentration $2.8 \times 10^{18}$ $cm^{-3}$) is close to our data. Thus, the continuous approximation is applicable to the superlattices with GaAs quantum wells of submonolayer width. However, this approach does not necessarily apply to the superlattices with thick GaAs layers. Whereas the phonon frequencies in solid solutions depend on the stoichiometric composition, the frequencies of optical phonons in the superstructure depend only on the thickness of the layers in which they are confined. The continuous model cannot always be used in calculating the dielectric constant and the phonon–plasmon interaction in superlattices, because the charge carriers and phonons may be spatially separated. It is also not improbable that the contribution of the coupled acoustic and interface modes to the dielectric constant cannot be ignored for the superlattices.

Thus, Raman scattering spectroscopy was used to experimentally observe mixed phonon–plasmon modes in thin tunneling GaAs/AlAs superlattices. The electronic levels are "expelled" from the GaAs quantum wells as the thickness of GaAs layers decreases, resulting in the strengthening of the interaction between plasmons and optical phonons localized in the AlAs layers. Raman scattering from the mixed phonon–plasmon modes was found to be more intense for the GaAs quantum islands and ruffled AlAs layers.

This work was supported by the Russian Foundation for Basic Research, project no. 99-02-16668. One of the authors (V.A.V.) is grateful to the Scientific Council of the Institute of Semiconductor Physics SD RAS for assistance in the form of awarding of the stipend for young scientists of the Institute of Semiconductor Physics SD RAS.

## REFERENCES

1. A. Pinczuk, G. Abstreiter, R. Trommer, and M. Cardona, Solid State Commun. **21**, 959 (1977).
2. S. Das Sarma and J. J. Quinn, Phys. Rev. B **25**, 7603 (1982).
3. D. Olego, A. Pinczuk, A. C. Gossard, and W. Weigmann, Phys. Rev. B **25**, 7867 (1982).
4. T. Egeler, S. Beck, G. Abstreiter, *et al.*, Superlattices Microstruct. **5**, 123 (1989).
5. L. Wendler and R. Pechstedt, Phys. Rev. B **35**, 5887 (1987).
6. A. Pinczuk, J. M. Worlock, H. L. Stormer, *et al.*, Solid State Commun. **36**, 43 (1980).
7. Yia-Chung Chang, H. Yao, and M. Mohiuddin, J. Appl. Phys. **85**, 1616 (1999).
8. *Light Scattering in Solids IV. Problems of Applied Physics*, Vol. 4: *Electronic Scattering, Spin Effects, SERS, and Morphic Effects*, Ed. by M. Cardona and G. Güntherodt (Springer-Verlag, New York, 1975; Mir, Moscow, 1984).
9. *Light Scattering in Solids*, Vol. 5: *Superlattices and Other Microstructures*, Ed. by M. Cardona and G. Güntherodt (Springer-Verlag, New York, 1989).
10. A. O. Govorov and A. V. Chaplik, Zh. Éksp. Teor. Fiz. **94** (12), 251 (1988) [Sov. Phys. JETP **67**, 2532 (1988)].
11. L. Friedman, Phys. Rev. B **32**, 955 (1985).
12. M. D. Efremov, V. A. Volodin, and V. V. Bolotov, in *Proceedings of the 21st International Conference on Physics of Semiconductors, Beijing, China, 1992*, p. 1072.
13. M. D. Efremov, V. A. Volodin, and V. V. Bolotov, Solid State Phenom. **32/33**, 583 (1993).
14. A. M. Mintairov, K. E. Smekalin, V. M. Ustinov, and V. P. Khvostikov, Fiz. Tekh. Poluprovodn. (Leningrad) **24**, 1539 (1990) [Sov. Phys. Semicond. **24**, 962 (1990)].
15. A. M. Mintairov, K. E. Smekalin, V. M. Ustinov, and V. P. Khvostikov, Fiz. Tekh. Poluprovodn. (St. Petersburg) **26**, 610 (1992) [Sov. Phys. Semicond. **26**, 347 (1992)].
16. K. Reginski, J. Muszalski, V. V. Preobrazhenskiĭ, *et al.*, Thin Solid Films **267**, 54 (1995).
17. M. D. Efremov, V. A. Volodin, V. A. Sachkov, *et al.*, Pis'ma Zh. Éksp. Teor. Fiz. **70**, 73 (1999) [JETP Lett. **70**, 75 (1999)].
18. C. Colvard, T. A. Gant, M. V. Klein, *et al.*, Phys. Rev. B **31**, 2080 (1985).

*Translated by V. Sakun*

*JETP Letters, Vol. 71, No. 11, 2000, p. 481.*

# Erratum: "Efficient Nonlinear-Optical Frequency Conversion in Periodic Media in the Presence of Diffraction of the Pump and Harmonic Fields" [*JETP Lett.* 70, 12, 811–818 (25 Dec. 1999)]

**V. A. Belyakov**

An error occurred in the abstract of this paper when the translation was provided by AIP. The first sentence of the abstract should begin with "It was predicted by Belyakov and Shipov [*Phys. Lett. A* **86**, 1867 (1972)] and observed by… ."

0021-3640/00/7111-0481$20.00 